



JÖNKÖPING UNIVERSITY

*School of Engineering*

Doctoral Thesis

# **Durability Evaluation of PEM Fuel Cell Components**

Live Mølmen

Jönköping University  
School of Engineering  
Dissertation Series No. 078 • 2023





JÖNKÖPING UNIVERSITY  
*School of Engineering*

Doctoral Thesis

# **Durability Evaluation of PEM Fuel Cell Components**

Live Mølmen

Doctoral Thesis in Materials and Manufacturing

Durability Evaluation of PEM Fuel Cell Components  
Dissertation Series No. 078

© 2023 Live Mølmen

Published by  
School of Engineering, Jönköping University  
P.O. Box 1026  
SE-551 11 Jönköping  
Tel. +46 36 10 10 00  
[www.ju.se](http://www.ju.se)

Printed by Stema Specialtryck AB, year 2023

ISBN 978-91-87289-88-0 (Printed version)  
ISBN 978-91-87289-89-7 (Online version)



# Abstract

Proton exchange membrane fuel cells (PEMFCs) are used to convert hydrogen and oxygen to electricity, heat, and water. There are no greenhouse gas emissions, given that the hydrogen is produced from renewable sources, such as water electrolysis from wind, hydro or solar energy. PEMFCs can be found on the commercial market today, predominantly in applications such as forklifts, passenger cars and combined heat and power units. The PEMFC is a new technology, and there are hurdles to overcome, mainly with regard to price and durability.

In this work, two PEMFC components are the main focus: the bipolar plate and the catalyst. For the bipolar plate, the effect of defects from fabrication is investigated to further understand the critical factors for corrosion and how to avoid it. Droplets from laser cutting and cracks in the coating due to the forming of pre-coated plates are both identified as possible sources of corrosion. However, by correct design, both can be avoided or made less critical. Laser welding stainless steel 304 is, on the other hand, found not to be a source of corrosion under simulated PEMFC bipolar plate conditions. Furthermore, tailoring the properties of a multicomponent alloy coating by additions of Ta and W is explored to stabilise the coating at higher potentials in the acidic environment of the PEMFC. Ta is found to achieve a protective passive layer at a lower concentration than W. However, it does significantly increase the interfacial contact resistance. One-step synthesis of a ternary alloy by electrodeposition is studied for the catalyst to allow for facile screening of new alloy compositions, both in- and ex-situ. The ternary alloy gives comparable results to the binary alloy even at lower Pt content.

As the PEMFC has entered the commercial market relatively quickly, there is a lack of standardised tests, both on the component and system level. The procedure for testing the interfacial contact resistance of the bipolar plate is studied in detail, and the methodology is further developed to ensure reliable and comparable results.

**Keywords:** Proton exchange membrane fuel cell, bipolar plate, corrosion, interfacial contact resistance, electrocatalysis

# Sammanfattning

Protonledande polymermembranbränsleceller (PEMFCs) används för att omvandla vätgas och syrgas till elektricitet, värme och vatten. Om vätgasen produceras på ett förnybart sätt, till exempel genom vattenelektrolys driven med sol, vind eller vattenkraft, sker det inga utsläpp av växthusgaser. Redan idag finns PEMFCs på den kommersiella marknaden. Huvudsakligen används de i applikationer som gaffeltruckar, personbilar och kraftvärmeapplikationer. Eftersom PEMFCs är en relativt ny teknik, finns det fortfarande ett behov för utveckling, speciellt när det kommer till kostnad och livslängd.

Två PEMFC komponenter har varit huvudfokus för detta arbete: den bipolära plattan och katalysatorn. För den bipolära plattan studeras effekten av defekter från produktionen på korrosionsbeständigheten. Både droppar av smält metall från laserskärning och sprickor i beläggningen från formning av förbelagd plåt kan initiera korrosion på den bipolära plattan. Dock, kan båda defekterna undvikas vid korrekt design av plattan. Däremot visar det sig att lasersvetsar i rostfritt stål 304 utan beläggning inte initierar korrosion i ett simulerat PEMFC-miljö. I tillägg utforskas möjligheten att utvidga det passiva området för en multikomponentlegering genom tillsatser av Ta och W. Ta bildar ett stabilt passivskikt vid lägre halter jämfört med W, dock ökar kontaktresistansen signifikant. För katalysatorn studeras elektroplätning av en ternär legering direkt på gasdiffusionsskiktet för enkel screening av nya legeringar för katalysatorn. Den ternära legeringen ger jämförbar prestanda med den binära, även vid låga Pt halter.

Allt eftersom PEMFC har kommersialiserats ökar fokuset på utveckling av standardiserade prov, både på komponent och systemnivå. Metodologin för att mäta kontaktresistansen för bipolära plattor vidareutvecklas i detta arbete för att säkra pålitliga och repeterbara mätningar.

**Nyckelord:** Polymermembranbränsleceller, bipolära plattor, korrosion, kontaktresistans, katalys

# Acknowledgements

I would like to express my gratitude to my main supervisor, Peter Leisner, for his support, patience and many great discussions. I am grateful to my supervisor at RISE, Lars Fast, for his guidance and for his thoroughness when it comes to problem-solving. I want to thank Caterina Zanella for the discussions on everything related to corrosion and Anders Lundblad and Annika Carlson for the discussions on everything related to fuel cells.

There would not have been any papers without the collaboration with Konrad Eiler, Eva Pellicer and Jordi Sort at UAB, Maria Lekka and Francesco Andreatta at UNIUD, León Zendejas Medina, Ulf Jansson and Leif Nyholm at Uppsala University, and Peter Eriksson, Mikael Sundin and Marie Ernstsson at RISE. It has been a privilege to work with you all!

I would also like to thank the industrial partners that have helped by sending samples for me to study and giving input as to what questions need answering.

I want to thank Johan Börjesson for his invaluable help with the SEM.

I acknowledge the funding from European Union's Horizon 2020 research and innovation program under the Marie Skłodowska-Curie Grant Agreement No. 764977, Swedish Foundation for Strategic Research (Project No. ARC19-0026), the ALUSAP project within the strategic innovation programme Metallic materials funded by Vinnova, Formas, and Energimyndigheten, the Smart Industry Sweden project funded by the Swedish Knowledge Foundation and RISE.

The road would have been much more boring without the company of colleagues both at RISE and JTH, and fellow PhD students in mCBEEs, PUSH and SIS.

Last but not least, I want to thank my friends, family, mamma, pappa and Knut, and my sambo Tobias for the love and patience through these years.

# List of original papers

## **Paper 1**

Recent advances in catalyst materials for proton exchange membrane fuel cells

*L. Mølmen, K. Eiler, L. Fast, P. Leisner & E. Pellicer*

Published in APL Materials, 9 (2021) 040702

## **Paper 2**

Oxygen reduction reaction and proton exchange membrane fuel cell performance of pulse electrodeposited Pt-Ni and Pt-Ni-Mo(O) nanoparticles

*K. Eiler, L. Mølmen, L. Fast, P. Leisner, J. Sort & E. Pellicer*

Published in Materials Today Energy 27 (2022) 101023

## **Paper 3**

Contact resistance measurement methods for PEM fuel cell bipolar plates and electrical contacts

*L. Mølmen, L. Fast, A. Lundblad, P. Eriksson & P. Leisner*

Published in Journal of Power Sources 555 (2023) 232341

## **Paper 4**

Extending the passive region of CrFeNi-based high entropy alloys by including Ta or W

*L. Zendejas Medina, L. Mølmen, E.M. Paschalidou, O. Donzel-Gargand, P. Leisner, U. Jansson & L. Nyholm*

Manuscript

## **Paper 5**

Corrosion of pre-coated anode bipolar plates for PEM fuel cells

*L. Mølmen, F. Andreatta, M. Lekka, L. Fast & P. Leisner*

Manuscript

## **Paper 6**

Corrosion analysis of laser-welded stainless steel PEM fuel cell bipolar plates

*L. Mølmen, C. Zanella, M. Ernstsson, L. Fast & P. Leisner*

Manuscript

# Contribution to appended papers

**Paper 1:** K. Eiler and I contributed equally to conceptualisation, literature search, writing and revision.

**Paper 2:** K. Eiler and I contributed equally to conceptualisation, experimental work, writing and revision.

**Paper 3:** I contributed to the conceptualisation and performed the major part of the experimental work, writing and revision.

**Paper 4:** I performed the interfacial contact resistance measurements and part of the electrochemical ageing, wrote the corresponding part of the paper, and contributed to the revision.

**Paper 5:** I contributed to the conceptualisation and performed the major part of the experimental work, writing and revision.

**Paper 6:** I contributed to the conceptualisation and performed the major part of the experimental work, writing and revision.

# List of abbreviations

AST	Accelerated stress test
CCM	Catalyst coated membrane
CV	Cyclic voltammetry
DOE	US Department of Energy
ECSA	Electrochemical surface area
EBSD	Electron backscatter diffraction
EDS	Energy dispersive x-ray spectroscopy
GDE	Gas diffusion electrode
GDL	Gas diffusion layer
HOR	Hydrogen oxidation reaction
ICP-MS	Inductively coupled plasma mass spectrometry
ICR	Interfacial contact resistance
LOM	Light optical microscopy
MEA	Membrane electrode assembly
MPL	Microporous layer
OCP	Open circuit potential
OCV	Open circuit voltage
ORR	Oxygen reduction reaction
PEMFC	Proton exchange membrane fuel cell
PFSA	Perfluorinated sulfonic acid polymer
PTFE	Polytetrafluoroethylene
PVD	Physical vapour deposition
RH	Relative humidity
RHE	Reversible hydrogen electrode
SEM	Scanning electron microscopy
SHE	Standard hydrogen electrode
TEM	Transmission electron microscopy
XPS	X-ray photoelectron spectroscopy
XRD	X-ray diffraction

# Table of Contents

<b>1. Introduction.....</b>	<b>1</b>
1.1. Proton exchange membrane fuel cells .....	2
1.2. Performance and durability .....	6
1.3. Research questions .....	7
<b>2. Theory .....</b>	<b>8</b>
2.1. Electrochemistry .....	8
2.2. PEM fuel cells .....	12
2.3. Catalysts.....	14
2.4. Materials for bipolar plates.....	17
2.5. Bipolar plate production .....	21
2.6. Interfacial electrical contact resistance measurements .....	23
2.7. Corrosion .....	24
2.8. Ex-situ corrosion testing.....	28
2.9. In-situ accelerated stress testing .....	32
<b>3. Research methodology .....</b>	<b>34</b>
3.1. Materials .....	34
3.2. Electrochemical experiments.....	36
3.3. PEMFC single cell.....	38
3.4. Interfacial electrical contact resistance measurements .....	40
3.5. Environmental durability .....	40
3.6. Materials characterisation.....	41
<b>4. Results and discussion .....</b>	<b>43</b>
4.1. Electrodeposited Pt-Ni and Pt-Ni-Mo .....	43

4.2.	Effect of passivation on the ICR.....	48
4.2.1.	Characterization of the coated samples .....	48
4.2.2.	Interfacial contact resistance methodology .....	49
4.2.3.	Initial coating comparison .....	53
4.2.4.	Ageing CrFeNiTa in H <sub>2</sub> SO <sub>4</sub> .....	55
4.2.5.	Ageing NiP and NiSn by environmental durability testing..	57
4.2.6.	Conclusions on ICR measurements and the effect of passivation on the ICR .....	59
4.3.	Localised corrosion on bipolar plates .....	60
4.3.1.	Precoated flow plates.....	60
4.3.2.	Laser welded stainless steel.....	66
4.3.3.	Conclusions on localised corrosion.....	69
<b>5.</b>	<b>Conclusions and future work .....</b>	<b>71</b>
	<b>References .....</b>	<b>75</b>

# 1. Introduction

In a report by the Intergovernmental Panel on Climate Change (IPCC)<sup>1</sup> hydrogen is one of several energy carriers pointed out as a key to balancing a fully electrified energy system. Furthermore, to reach the target of only 1.5°C global warming by 2050, the CO<sub>2</sub> emissions from the transport sector must be reduced by 59% compared to 2020. Hydrogen is one of the solutions to reduce emissions from transport for both land, aviation, and shipping<sup>1</sup>. As of November 2022, 26 governments have established hydrogen strategies, and the G7 countries launched the Hydrogen Action Pact in May 2022<sup>2</sup>. Hydrogen is part of the Breakthrough Agenda launched at COP 26 in November 2021 in Glasgow. The need for a rapid upscaling in renewable hydrogen production and the increased usage of hydrogen in industrial and heavy-duty vehicle applications are some of the recommendations in the Breakthrough Agenda Report 2022<sup>3</sup>.

Battery electric vehicles are already taking large market shares in the light vehicle segment. There is, however, uncertainties in the heavy-duty vehicle segment about both weight and charging time for pure battery electric vehicles. Adding a hydrogen fuel cell can reduce the weight of the vehicle as only the hydrogen tank scales up with the range, and it furthermore allows for quick refuelling<sup>4</sup>. There are several types of hydrogen fuel cells, but the proton exchange membrane fuel cell (PEMFC) is the most commercially advanced type for vehicle applications due to the relatively low operating temperature and the compactness of the system<sup>5</sup>. In 2021, the number of fuel cell electric vehicles (FCEVs) surpassed 50 000, with South Korea having the most FCEVs on the road, followed by the USA, China, and Japan<sup>6</sup>. 80% of the FCEVs on the road today are personal cars<sup>6</sup>, but heavy-duty vehicles are expected to take a larger market share in the near future<sup>4</sup>. To reach broader commercialisation, the lifetime of the PEMFC must be improved while at the same time reducing cost.

## 1.1. Proton exchange membrane fuel cells

The proton exchange membrane fuel cell is a multilayer system consisting of a polymer membrane in the centre. On each side, there is a catalyst layer, a gas diffusion layer (GDL), and a bipolar plate<sup>5,7</sup>, see Figure 1.

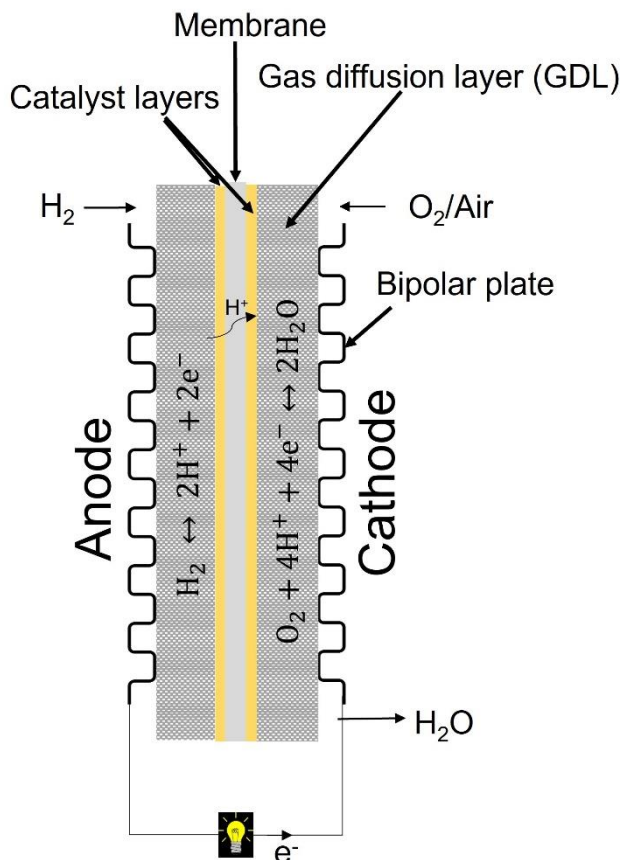
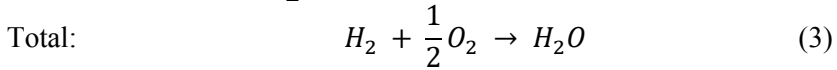
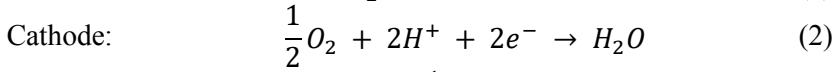
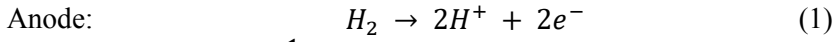
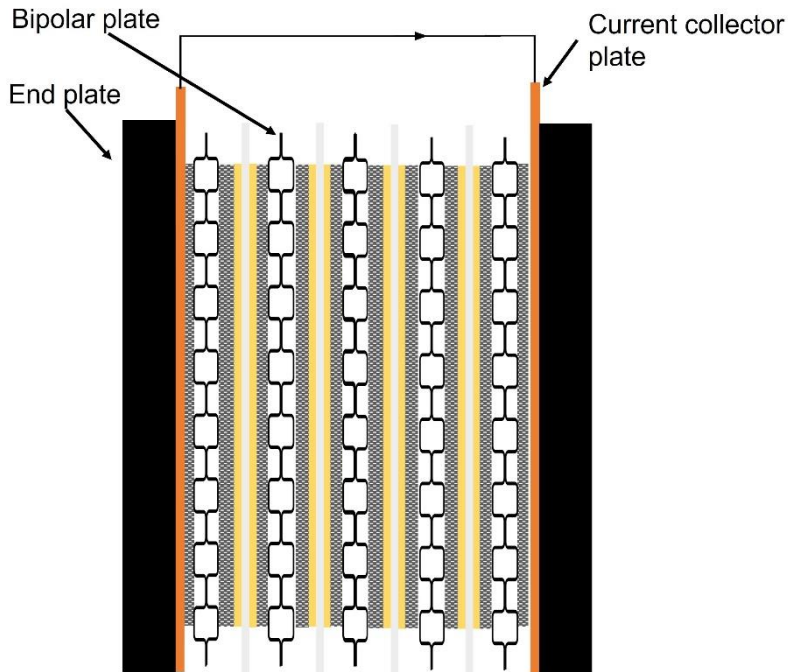


Figure 1: A schematic illustration of a PEMFC single cell

At the catalyst layers on either side of the membrane, the two half-reactions occur. Hydrogen is split into a proton and an electron on the anode side. The proton is transported through the membrane while the electron goes through the outer circuit. The proton and the electron react with oxygen on the cathode side to form water. The total reaction is:



The reversible open circuit potential at room temperature of the total reaction is 1.23 V. However, there will always be losses due to activation, ohmic resistances and mass transport. Thus, the measured voltage of a fuel cell is always lower, typically operating between 1.0-0.5 V <sup>7</sup>. To achieve sufficient energy output to power a vehicle, several hundreds of cells are stacked in series<sup>8</sup> (Figure 2). There are additional components when assembling the stack, such as cooling channels in the bipolar plates, current collector plates that connect the end of the stack to the outer circuit, and end plates for mechanical support. Each cell is sealed with gaskets.



*Figure 2: Schematic illustration of a cross section of a PEMFC stack containing four single cells as shown in Figure 1 connected in series.*

The type of PEMFC on the commercial market is the low-temperature PEMFC, which operates at 60-90°C, limited by the need to humidify the membrane, which requires humidification to achieve high proton conductivity. It is this type of PEMFC that will be discussed in this thesis. There is, however, a push toward higher operating temperatures, as this is more suitable for heat management in vehicles where a particular temperature difference is needed to operate heat exchangers. At intermediate temperatures (80-120°C), the humidity can be stabilised by increasing the operating pressure, or by adding additives to the membrane to be able to operate at lower relative humidity<sup>9</sup>. Above 120°C, other membrane chemistries are required<sup>10</sup>.

## The membrane

The membrane in the low-temperature PEMFC is made of perfluorinated sulfonic acid polymer (PFSA)<sup>5,7</sup>. While the backbone of the polymer is hydrophobic, the sulfonic acid functional groups are hydrophilic. As the membrane absorbs water, the hydrophilic groups will cluster together. Upon applying a potential over the membrane, the water clusters will form proton conductive pathways through the membrane<sup>7</sup>. A PEMFC must be conditioned at the beginning of life to allow for the humidification of the membrane and the reordering of the sulfonic acid functional sites.

PFSA has both high proton conductivity and is durable. When the membrane degrades, the polymer is split, and fluoride ions can be released. The degradation of PFSA is accelerated by Fenton's reaction. In Fenton's reaction, H<sub>2</sub>O<sub>2</sub> is produced by O<sub>2</sub> crossover to the anode. The H<sub>2</sub>O<sub>2</sub> further split to form hydroxide radicals that attack the polymer. The Fenton reaction is catalysed by ions of Fe and other metals<sup>11,12</sup>. Therefore, it is critical that metal ion contamination of the membrane is minimised to achieve a long lifetime of the PEMFC. Several additions can be made to the membrane to increase its lifetime, such as SiO<sub>2</sub> to bind more water in the membrane, polytetrafluoroethylene (PTFE) as mechanical reinforcement, and CeO<sub>2</sub> as a radical scavenger to reduce degradation<sup>13,14</sup>.

## The catalyst layers

The most used catalyst for PEMFCs is Pt. The catalyst layer constitutes 41% of the PEMFC system cost due to the price of Pt<sup>15</sup>. Thus, there is a push to

reduce or eliminate the use of Pt. To utilise as much of the Pt as possible, the catalyst layer consists of Pt nanoparticles supported on carbon<sup>16</sup>. This way, the Pt surface area is maximised, and the carbon ensures electrical contact. The goal set by the US Department of Energy (DOE) for 2050 is a Pt, or Pt group metal, loading of less than 0.1 mg/cm<sup>2</sup>, which would give a total Pt loading of around 10 g for an automotive-size PEMFC stack, comparable to the platinum group metal content found in a catalytic converter for a diesel engine (7-10 g)<sup>15,17</sup>. Furthermore, for reactions (1) and (2) to occur, there must be a proton conductive media from the catalyst surface to the membrane. Therefore, a thin layer of ionomer, commonly PFSA, is added to the catalyst layer<sup>18</sup>.

At the anode, the Pt loading can be very low without affecting the PEMFC performance. The cathode reaction is a multistep reaction and is therefore slower; thus, a higher catalyst loading is necessary<sup>16</sup>. Furthermore, the durability of the cathode catalyst is a problem due to the oxidising environment. Alloying Pt with transition metals such as Co and Ni is a common strategy to reduce Pt loading<sup>16</sup>.

The catalyst layer is prepared as ink and sprayed onto the membrane to form a catalyst-coated membrane (CCM) or sprayed onto the GDL to form a gas diffusion electrode (GDE). Together, the membrane, catalyst layers and GDLs form what is described as the membrane electrode assembly (MEA).

### The gas diffusion layer

The GDL is a two-part layer consisting of a backing layer and a microporous layer (MPL)<sup>7</sup>. It has several functions in the PEMFC, including reactant and product transport, electrical conduction, mechanical support, and thermal management<sup>5,19,20</sup>. The backing layer is a porous structure made of carbon fibres and can be both woven and non-woven<sup>20</sup>. To aid in removing water from the PEMFC, the backing layer is often treated with PTFE to increase the hydrophobicity<sup>20</sup>.

The MPL is added to improve contact with the catalyst layer<sup>20,21</sup>. It consists of carbon particles and PTFE<sup>20,22</sup>. To aid in the water removal from the catalyst layer, the PTFE content is higher in the MPL than in the backing layer<sup>23,24</sup>. The MPL can penetrate into or be on top of the backing layer<sup>24</sup>.

## The bipolar plate

The bipolar plates have several functions in the PEMFC stack. They separate neighbouring cells, distribute the gases between cells and over the active area, remove produced water, conduct electricity, support mechanically, and have built-in cooling channels to control the temperature<sup>25</sup>. Graphite is commonly used for bipolar plates as it has excellent chemical stability in the PEMFC environment<sup>25,26</sup>. However, since machining flow fields for gas distribution is expensive<sup>26</sup>, and thicker plates are needed to achieve mechanical strength as well as to ensure that no porosity penetrates the plate<sup>25</sup>, graphite is not the material of choice for vehicle application where cost, weight and volume are all important factors.

Metallic materials such as titanium and stainless steel have high mechanical strength, and cost-effective mass production of formed plates is possible<sup>26</sup>. However, the chemical stability and interfacial contact resistance (ICR) of metallic bipolar plates need to be addressed<sup>25,27</sup>. Acidic and humid environments, as that of the PEMFC, are corrosive<sup>28,29</sup>. The metals that are stable in such an environment form an oxide on the surface, as is the case for both stainless steel and titanium<sup>27</sup>. The surface oxide increases the ICR<sup>30–32</sup>. As there are several hundred bipolar plates in the PEMFC stack, a slight increase in the ICR of each will have a sizeable accumulative effect. Thus, protective, conductive coatings are needed<sup>25,26</sup>.

## 1.2. Performance and durability

PEMFCs are still a new technology on the commercial market. As more companies start offering PEMFC components and systems, the importance of standardised and harmonised testing is apparent. The measurements can be divided into ex-situ and in-situ, where ex-situ measurements are performed outside of the PEMFC on a single component, and in-situ measurements are performed in a PEMFC, either single cell or stack. The testing should include both performance and durability. In the case of durability measurements, there is a need to accelerate the degradation to give valuable information without testing the full lifetime. It is, however, important to be careful when deciding how to accelerate the degradation so that the degradation mechanism is not changed. In the ex-situ testing, the properties of the material can be

quantitatively determined. However, care must be taken that the measurement environment accurately simulates the PEMFC environment. In-situ testing is closer to normal operation, but it can be difficult to connect performance loss with a specific performance or material characteristic.

### 1.3. Research questions

The aim of the thesis has been to study how the metallic components in the PEMFC degrade and how the degradation can be both monitored and mitigated. Based on the literature study, conversations with the industry, and results from the initial work, four research questions have been formulated:

**RQ1:** How can the Pt catalyst durability be increased while reducing the amount of Pt? (Paper 1 and 2)

**RQ2:** How can interfacial contact resistance be measured with high reliability and validity? (Paper 3 and 4)

**RQ3:** What are the critical points for localised corrosion on PEMFC bipolar plates? (Paper 5 and 6)

**RQ4:** How can the degradation mechanisms be detected after in-situ ageing in a PEMFC? (Paper 2 and 5)

The papers related to each research question are indicated above. In the next chapter, the theory and background will be given. In the third chapter, the experimental setups are described in brief. For detailed descriptions, the reader is referred to the appended papers. In chapter four the experimental results are presented and discussed and set into the context of the research questions. Finally, chapter 5 concludes the thesis with a summarising discussion and recommendations for further work.

## 2. Theory

In the following chapter, the theoretical background for the work performed will be described, as well as an overview of state of the art within the different topics.

### 2.1. Electrochemistry

Electrochemical reactions are chemical reactions that involve the transfer of electrons. The electrochemical reactions always consist of two half-reactions. One oxidation reaction, in which electrons are released, and one reduction reaction, where electrons are consumed. The place at which the oxidation reaction occurs is defined as the anode, and the place at which the reduction reaction occurs is defined as the cathode<sup>33</sup>. In the PEMFC described in section 1.1, reaction (1) is the oxidation reaction and thus the anode reaction, and reaction (2) is the reduction reaction and therefore the cathode reaction. The total reaction is given by reaction (3)<sup>7</sup>. Also electrodeposition and corrosion are electrochemical processes that are studied in this work.

#### Thermodynamics

As for all chemical reactions, the maximum amount of work obtainable from a reaction is found by the change in Gibbs free energy, which for a reaction is defined by:

$$\Delta_r G = \Delta_r H - T\Delta_r S \quad (4)$$

A reaction is spontaneous if the change in Gibbs free energy is negative. Energy needs to be added to a system for reactions to occur when the change in Gibbs free energy is positive. At equilibrium, the change in Gibbs free energy is equal to zero<sup>33</sup>.

In electrochemical reactions, electrical work can be defined as the charge multiplied by the potential. As a maximum, the electrical work must be equal to the work of the chemical reaction. Thus, the equilibrium potential can be found by:

$$\Delta_r G = -nFE_0 \quad (5)$$

where  $n$  is the number of electrons transferred in the reaction,  $F$  is the Faraday number, and  $E_0$  is the equilibrium potential<sup>33</sup>.

When looking up thermodynamic data, the values are given at standard temperature and pressure, with activities of all species equal to one. When not working at standard conditions, the equilibrium potential is given by the Nernst equation:

$$E = E^0 + \frac{RT}{nF} \ln \frac{a_{prod}}{a_{react}} \quad (6)$$

where  $E^0$  is the potential at standard conditions, and  $a$  is the activity of products and reactants<sup>33</sup>.

## Kinetics

The thermodynamics give the potential of a system when it is at equilibrium. In such a case, no current is passing through the system. When a current is applied over the electrochemical system, the potential will deviate from the equilibrium potential. The difference between the measured potential and the equilibrium potential is defined as the overpotential,  $\eta$ . There are several sources for the overpotential, including charge transfer overpotential and diffusion overpotential.

An electrochemical half-reaction can go either in the anodic or the cathodic direction. At equilibrium, the net current is zero. However, the reactions may still take place as long as the anodic and cathodic partial current densities are equal. This current density is called the exchange current density. The total current of a reaction limited by the charge transfer can be calculated by the Butler-Volmer equation:

$$i = i_0 \left[ \exp \left\{ (1 - \beta) \frac{nF\eta}{RT} \right\} - \exp \left\{ -\beta \frac{nF\eta}{RT} \right\} \right] \quad (7)$$

where  $i_0$  is the exchange current density and  $\beta$  is the asymmetry factor<sup>33</sup>. The first exponential represents the anodic current, and the second represents the cathodic current. At high overpotentials, one term will be significantly larger than the other, and the minor term becomes negligible. Taking the cathode as

an example, the overpotential will be negative and significantly large so that the first exponential in equation (7) becomes negligible. The current can then be written as:

$$i = -i_0 \exp\left\{\frac{-\beta n F \eta}{RT}\right\} \quad (8)$$

Which can be rearranged to give the overpotential as a function of current:

$$\eta = A + B \log_{10}|i| \quad (9)$$

which is the Tafel equation<sup>33</sup>. A is a constant, and B is the Tafel slope given by:

$$A = \frac{2.303RT}{\beta n F} \log_{10}|i_0| \quad (9a) \quad B = \frac{-2.303RT}{\beta n F} \quad (9b)$$

## Reference electrodes

When studying electrochemical reactions, the focus is most of the time on either the oxidation or the reduction reaction. In the PEMFC, the performance is measured as the cell voltage, i.e. the voltage difference of both the oxidation and reduction reaction combined. In systems with liquid electrolytes, a reference electrode can be added. By measuring the voltage difference between the reference electrode and the electrode where the reaction of interest is occurring, called the working electrode, the potential of the working electrode can be determined. To determine the potential, the zero value must be known, and for electrode potentials, the standard hydrogen electrode (SHE) is defined as the zero potential electrode. In the SHE, hydrogen is evolved:



The reaction occurs on a Pt electrode immersed in a solution in which  $H^+$  has an activity of one and is in contact with hydrogen gas at one atmosphere pressure. Knowing that the SHE has a potential of 0 V, all other half reactions can be characterised by measuring the potential difference between the SHE and the working electrode. In reactions where there is a current being passed, the current is passed between the working electrode and a separate counter electrode so that no current is passing through the reference electrode. This is

done so that no overpotentials of the reference electrode interfere with the measurement.

Although the SHE is defined as the zero potential reaction, and the potentials of all other reactions are given with respect to the SHE, there are practical limitations to the set-up of the SHE, which results in other reference electrodes being used in practice. The closest to the SHE is the reversible hydrogen electrode (RHE), which is still based on reaction (10), but at a different pH than 0, thus, the proton activity is not one. The potential of the RHE can be calculated by the Nernst equation (equation 6). At pH 0.29, corresponding to 0.5 M H<sub>2</sub>SO<sub>4</sub>, the shift is only -0.0017 V vs SHE, while it for pH 2.73, corresponding to 1 mM H<sub>2</sub>SO<sub>4</sub>, is -0.162 V vs SHE. In this work, the commonly used Ag/AgCl reference electrode is utilised. This is not dependent on any gas phase, thus is simpler to handle. The Ag/AgCl reference electrode has a potential of:

$$E_{Ag|AgCl} = E_{Ag|AgCl}^0 - \frac{RT}{F} \ln a_{Cl^-} \quad (11)$$

The shift for Ag/AgCl in a solution of 3M KCl is 0.207 V vs SHE<sup>34</sup>. An overview of the relationship between reference electrodes relevant to this work is shown in Figure 3.

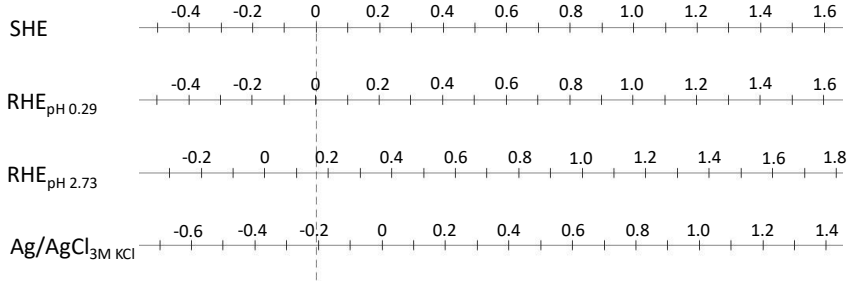


**Figure 3: The relationship between the potential (V) measured for different reference electrodes relevant to the present work.**

## 2.2. PEM fuel cells

As mentioned, reaction (3) has a theoretical equilibrium voltage of 1.23 V at room temperature. At 80°C, the operating temperature of the PEMFC, the Gibbs free energy of reaction (3) is reduced<sup>7</sup>, leading to an equilibrium voltage of 1.18 V. In addition, there are losses related to activation, crossover, ohmic resistances and mass transport, all of which are dependent on the applied load. It is, therefore, common to characterise the PEMFC by the polarization curve. An example of a polarization curve can be seen in Figure 4, where the contribution of the different losses is illustrated as separate curves.

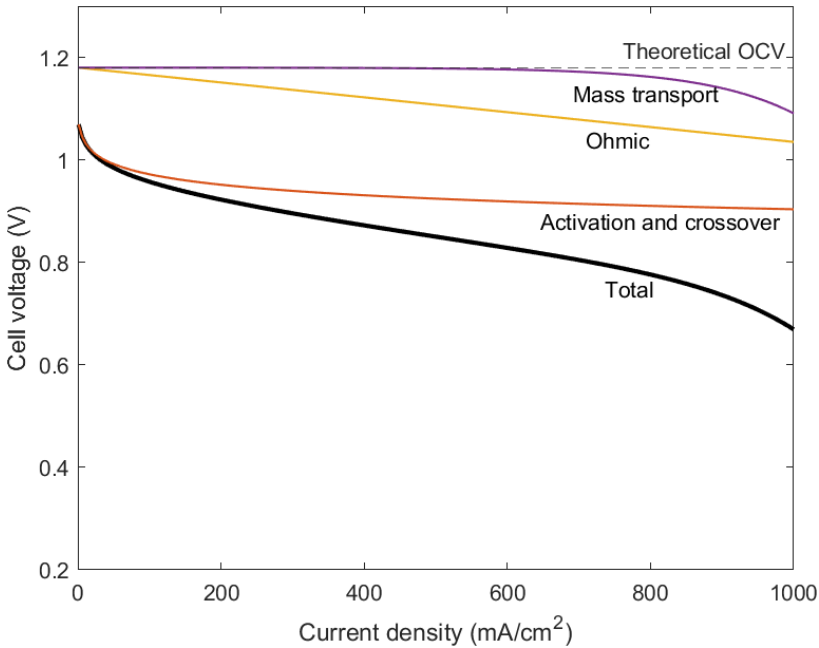


*Figure 4: Schematic polarization curve of a PEMFC operating at 80 °C, showing the theoretical OCV, overpotential losses representing mass transport (purple), ohmic (yellow) or activation energy and hydrogen crossover (red) separately. The total polarization curve (black) is shown with all losses incorporated, based on Larminie and Dicks<sup>7</sup>.*

The activation loss is related to the charge transfer at the electrode surface. It is described by equation (7), the Butler-Volmer equation. As can be seen in Figure 4, the activation loss dominates the polarization curve at low current

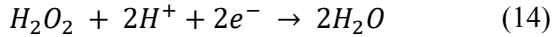
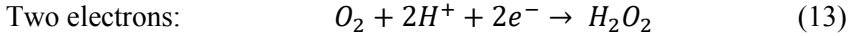
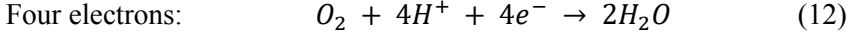
densities. One method to decrease the activation losses of the PEMFC is to maximise the surface area of the catalyst. The electrochemical active surface area (ECSA) is, therefore, one of the main criteria when optimising the catalyst. Due to the thin membrane in the PEMFC, and no membrane being entirely impermeable, some hydrogen will diffuse from the anode to the cathode compartment, causing crossover losses. In addition to causing loss of hydrogen at the anode side, the hydrogen will react with the oxygen at the cathode. The losses due to crossover correspond to a small current, only some  $\text{mA}/\text{cm}^2$ , but is noticeable as it significantly reduces the voltage at zero current, also called the open circuit voltage (OCV) of a PEMFC<sup>7</sup>. This is due to the activation loss related to the crossover current, and the two are therefore plotted together in Figure 4.

After the initial part of the polarization curve where the activation is dominating, the activation region, the polarization curve is linear. The linear region is often referred to as the ohmic region of the polarization curve. The ohmic losses originate from ohmic resistances in the cell. The ohmic loss increases linearly with the applied load in accordance with Ohm's law<sup>7</sup>. The ohmic loss is a combination of the membrane resistance related to proton conduction, bulk electrical resistances of GDLs, bipolar plates, current collector plates and wires, and the ICR between these components. Netwall et al.<sup>35</sup> studied the origin of ohmic losses in the PEMFC and found that 45% are related to bulk resistances, predominantly from the CCM, while 55% of the ohmic losses are caused by ICR.

Lastly, the PEMFC may experience mass transport losses at high loads. The mass transport losses may have different origins. The first, which is common in many systems, is a mass transport limitation above which the current cannot be increased as all of the reactants are consumed. Before this point is reached, a decrease in voltage is observed as the partial pressure of the reactant gases decreases. In addition to this, the accumulation of produced water may hinder the transport of reactants to the electrode<sup>7</sup>. This causes the polarization curve to drop at high current densities.

## 2.3. Catalysts

A catalyst greatly increases the rate of a reaction while not being consumed or altered<sup>33</sup>. The catalyst layers of the PEMFC are complex structures of carbon-supported Pt or Pt alloy nanoparticles, ionomer, and porosity. It is the Pt or Pt alloy that is the catalyst for both the hydrogen oxidation reaction (HOR) (reaction 1) and the oxygen reduction reaction (ORR) (reaction 2). The reactions can only occur if there is an electron conductor, proton conductor and reactants available. Thus, you need the catalyst particle, ionomer, and porosity all in contact at what is called a triple-phase boundary<sup>7</sup>. The catalyst is often, in practice, covered in a thin layer of ionomer, which the reactant gases can diffuse through<sup>18</sup>. As mentioned, the anode reaction, the HOR, is the fastest of the two half-reactions. The ORR, which takes place on the cathode catalyst, is more sluggish due to it requiring multiple electrons to be transferred and is the source of the large activation overpotential<sup>36</sup>. The reaction mechanism can either be a direct four-electron pathway (reaction 12) or divided into two steps, each with two electrons being transferred (reactions 13 and 14)<sup>33</sup>:



Which of the two pathways that will be dominating is dependent on the catalyst. The four-electron pathway is preferred as the hydrogen peroxide that is produced in reaction (13) is not all reduced further to water. Instead, the hydrogen peroxide may react through Fenton's reaction to form hydroxide radicals which degrade the membrane<sup>12–14,37</sup>.

Pt has been proven to have the highest catalytic activity for ORR among the pure metals<sup>36</sup>. The activity of Pt is again dependent on particle size and shape<sup>16,38</sup>. Shao et al.<sup>39</sup> concluded that the activity is highest for a Pt particle size of 3 nm. It has been shown that the Pt (111) facet has the highest activity towards ORR of the low-index facets. The fabrication of octahedra with (111) sides has therefore been studied<sup>38,40–42</sup>, along with more complex shapes such as the dumbbell<sup>43</sup>, to favour edges and steps that improve the catalytic activity.

Durability is one of the major issues for the catalyst layer. There are several mechanisms that contribute to catalyst degradation, including Pt dissolution, Ostwald ripening, where small particles dissolve and redeposit on bigger particles, particle migration and coalescence, and carbon support degradation<sup>44,45</sup>(Figure 5). Common for both Ostwald ripening and coalescence is that the particle size will increase. He et al.<sup>46</sup> found in a recent study that the average Pt particle size on the cathode side was four times as large after 1800 hours of vehicle operation, significantly reducing ECSA.

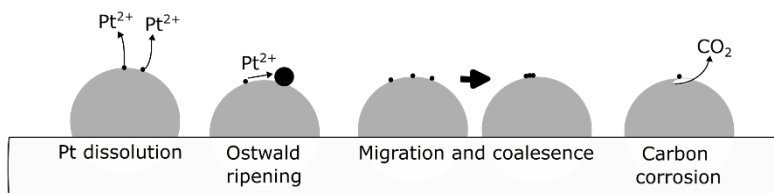
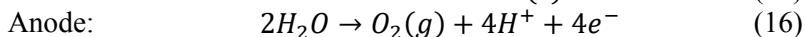
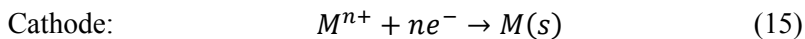


*Figure 5: Schematic illustration of catalyst degradation mechanisms.*

To reduce the Pt loading, alloying is a common strategy<sup>5,16</sup>. As cost reduction is one of the main driving forces, more abundant transition metals such as Ni<sup>40,41,47–53</sup> and Co<sup>54–58</sup> are the most common alloying element, although rare earth metals<sup>59,60</sup> and other noble metals<sup>61–64</sup> also are studied. While binary alloys are the most common, adding multiple alloy elements has gained focus in recent years to achieve both high activity and durability<sup>65–70</sup>, such as adding Mo to PtNi alloys<sup>40,71,72</sup>.

The Pt or Pt-alloy catalyst can be synthesised in many ways, with solvothermal reduction being the most common<sup>73–75</sup>. Physical vapour deposition (PVD) has been proposed as a simple synthesis method to screen different alloy compositions where the catalyst can be deposited directly on the GDL. However, the resulting catalyst is a thin film instead of nanoparticles<sup>59</sup>. The advantage of synthesising the catalyst directly on the GDL is that it allows for direct characterisation both ex-situ in a liquid electrolyte and in-situ in a PEMFC. Another synthesis method that can produce the catalyst directly on the GDL is electrodeposition. In electrodeposition, an electric charge or potential is applied between the substrate as a working electrode and a counter electrode, while a reference

electrode is used to monitor and control the deposition<sup>33</sup>. All three electrodes are submerged in an electrolyte containing dissolved salts of the metal to be deposited. The electrochemical reactions for the electrodeposition of a metal M are given by:



As can be seen, the anode reaction, in this case, is the oxygen evolution reaction. By adding several metal salts, an alloy can be formed by co-deposition. Tailoring the applied potential or current can alter the composition of the alloy<sup>49</sup>. As mentioned, electrodeposition can be performed either by controlling the current or the potential, called galvanostatically or potentiostatically, respectively. Furthermore, pulses can be used to tailor the deposition. Pulsed electrodeposition favour nucleation by applying high deposition currents or overpotentials. Depletion of the electrolyte closest to the working electrode is avoided by applying the off-time so that ions from the bulk can diffuse to the electrode surface<sup>76,77</sup>. The large overpotential in pulsed electrodeposition can furthermore favour the deposition of less noble metals during co-deposition. Huang et al.<sup>78</sup> produced Pt nanoparticles by pulsed current electrodeposition and achieved higher ORR activity at a lower loading as compared to the commercial Pt/C. Egetenmeyer et al.<sup>77</sup> successfully synthesised Pt, PtNi and PtCo by pulsed current electrodeposition with a crystallite size of 2-5 nm.

There is also work to synthesise catalysts without any noble metal additions. The most promising of these are the single-atom catalysts based on a carbon lattice doped with nitrogen and a transition metal, described as M-N-C, where M is the transition metal, most commonly Fe<sup>79-85</sup> or Co<sup>86-88</sup>. However, more research is still needed to reach similar performance and durability as the commercial Pt/C.

Paper 1 describes the recent advances within the research on PEMFC cathode catalysts in more detail.

## 2.4. Materials for bipolar plates

The combination of a humid environment, low pH, and an applied potential limit the choice of materials for the bipolar plate. Graphite is chemically stable. However, the brittle nature requires thicker plates, and expensive machining makes it unsuitable for automotive applications<sup>25,26,89,90</sup>. Metals, on the other hand, are mechanically strong, and manufacturing from sheet metals can be integrated into an assembly line and thus allow for cost-effective mass production<sup>90</sup>. The chemical stability is, however, an issue, especially when combined with the requirement of low ICR<sup>26,35</sup>.

The thermodynamic stability of an element can be seen in the Pourbaix diagram. This shows if the given metal in its bulk form is thermodynamically stable as a metal, a solid oxide, or a dissolved ion as a function of potential and pH<sup>91</sup>. Horizontal and diagonal lines are calculated from the Nernst equation (equation 6), while vertical lines are purely chemical reactions and are calculated by  $\Delta G_r = 0$ . The Pourbaix diagram does, however, not consider kinetic parameters for the transition between the different states. Hinds et al.<sup>29</sup> determined that the bipolar plate on the cathode side experiences a potential of around 0.6 V vs RHE. Measurements of the pH of the effluent water of the PEMFC vary between pH 3-7<sup>29,92</sup>. Pourbaix diagrams for selected metals relevant to the current work with a marking of the environment for the PEMFC cathode bipolar plate are shown in Figure 6. It can be seen that both Ni and Al can be found as  $\text{Ni}^{2+}$  and  $\text{Al}^{3+}$ , respectively, and thus will dissolve. The Fe is on the transition between  $\text{Fe}_2\text{O}_3$  and  $\text{Fe}^{2+}$ , thus will either dissolve or form an oxide layer. Also, Cr, which forms a stable passive oxide of  $\text{Cr}_2\text{O}_3$  at neutral pH, may dissolve either as  $\text{Cr}^{3+}$ ,  $\text{CrOH}^{2+}$  or form  $\text{Cr}_2\text{O}_3$ . Thus, all of these metals require a protective coating to avoid corrosion. Ta, on the other hand, forms the stable passive  $\text{Ta}_2\text{O}_5$ . Although corrosion of Ta will not be an issue due to the stability of the oxide, the electrical conductivity of the oxide is lower, so the ICR will be an issue<sup>93</sup>. Finally, Pt is in a stable metallic state and will provide low ICR and high corrosion resistance. However, Pt is far too expensive to be used for the entire bipolar plate.

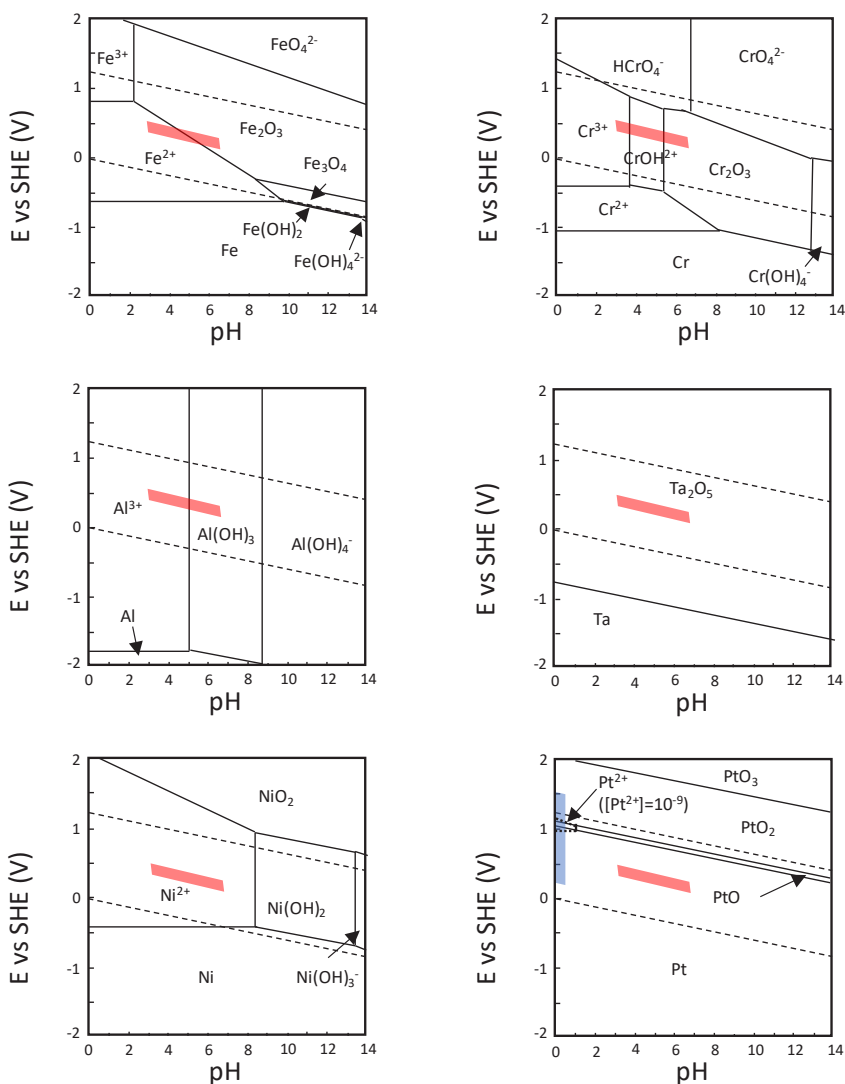


Figure 6: Pourbaix diagrams of Fe, Cr, Al, Ta, Ni and Pt, with the area representative of the PEMFC environment marked in red. For Pt, the area representative of the catalyst is marked in blue. All Pourbaix diagrams are based on calculation from the Hydra/Medusa software<sup>94</sup>, except for Ta, which is based on the Atlas of Electrochemical Equilibria in Aqueous Solutions by M. Pourbaix<sup>91</sup>. All ionic concentrations are  $10^{-6}$  M, and the temperature is 25 °C.

Stainless steels are Fe-based alloys that, through alloying, forms a passive surface film, limiting the amount of corrosion under “normal” conditions. The main alloying element is Cr. A minimum of 10.5wt% Cr is needed to form a stable passive film and therefore improve corrosion resistance<sup>95</sup>. A stainless steel is defined as an alloy containing at least 50wt% Fe, more than 10.5wt% Cr and a maximum of 1.2wt% C. There are a wide variety of stainless steels, classified by their microstructure; austenitic, ferritic, martensitic, duplex and precipitation-hardened stainless steels. The austenitic stainless steels show high corrosion resistance, can be hardened and welded, and are ductile and temperature resistant<sup>95</sup>. The austenitic stainless steels are, therefore, the most common choice for PEMFC bipolar plates. In addition to Cr, several other alloying elements are added. Ni is the most abundant alloying element after Cr and increases corrosion resistance in an acidic environment. Furthermore, Ni stabilises the austenitic phase and is therefore added in a considerable amount in the austenitic stainless steels<sup>95</sup>. Mo is added to avoid localised corrosion, such as pitting and crevice corrosion<sup>95</sup>. Mn increases the ductility, and the solubility of N. Cu will also improve the corrosion resistance as long as it is in solid solution. However, care must be taken, as Cu precipitates may instead leave the steel sensitive to pitting corrosion<sup>96</sup>. Si increases oxidation resistance. C is also an austenite stabiliser. However, too high C will decrease the resistance to intergranular corrosion and pitting, and the C content is therefore reduced in some stainless steels, such as 316L. N is another austenite stabiliser as well as increases mechanical strength and resistance to localised corrosion<sup>31,97</sup>. P improves strength and machineability but has a negative effect on corrosion resistance and weldability<sup>95</sup>.

The compositions of some austenitic stainless steels commonly used for PEMFC are given in Table 1. The most common stainless steel used in PEMFC bipolar plates is AISI 316L, also called EN 1.4404 or 1.4435, dependent on Mo and Ni content, with 1.4435 having a higher level of alloying elements. The suitability of 316L and other austenitic stainless steels for PEMFC applications has been thoroughly studied in the literature<sup>98–106</sup>. Kumagai et al.<sup>32</sup> studied the effect of pH on the surface oxide composition of 310S. They found that there is a transition between pH 3–4, where samples exposed to a pH 4 or higher had an iron-rich oxide layer, while the oxide layer was chromium rich after exposure at pH 3 and lower. Comparison to a bipolar plate of the same stainless steel after 1000 hours on the cathode side of a

PEMFC showed that the centre and gas inlet still had the iron-rich oxide, while the gas outlet appeared to have been exposed to a lower pH and therefore had a more chromium-rich oxide<sup>32</sup>. Li et al.<sup>102</sup> found a positive effect of strain on the corrosion resistance of 316L due to an increased amount of Cr<sub>2</sub>O<sub>3</sub> in the surface oxide after deformation. Even though several works report how to improve the corrosion resistance of austenitic stainless steel, the growth of the oxide layer, which is the basis of the protective strategy, will lead to an increase in ICR. An overview of contact resistance and corrosion resistance of different stainless steel by Leng et al.<sup>107</sup> shows that although single measurements on some steels meet the requirements for PEMFC bipolar plates, no steel grade consistently meets the targets.

**Table 1: The composition in wt% of some common stainless steels for PEMFC application<sup>107,108</sup>. Fe is added to balance.**

AISI	Cr	Ni	Mo	C	N	Si	Mn	P	S	Cu
304	18-20	8-10.5	-	0.08	0.10	0.75	2.0	0.045	0.030	-
310S	24-26	19-22	-	0.08	-	1.5	2.0	0.045	0.030	-
316	16-18	10-14	2.0-3.0	0.08	0.10	0.75	2.0	0.045	0.030	-
316L	16-18	10-14	2.0-3.0	0.03	0.10	0.75	2.0	0.045	0.030	-
904L	19-23	23-28	4-5	0.02	0.10	1.00	2.0	0.045	0.035	1-2

Due to the fact that no one pure metal or alloy meets the criteria for corrosion resistance, ICR and cost, coatings are applied on the bipolar plates. Stainless steel and titanium are the two most common substrate materials for coated metal bipolar plates<sup>26,90</sup>. One alternative is to use Pt as a coating, as has been done in many early commercial PEMFCs for vehicles, among others, in the Toyota Mirai<sup>8</sup>. The total area of the bipolar plates is, however, sufficiently large so that it is not feasible to coat even thin layers of Pt without exceeding the limit of what is economically sound. Also Au has been utilised, limiting the thickness to the nanometre scale to reduce the cost<sup>109</sup>. There is, however, a large amount of ongoing research to find more cost-effective coatings. Metallic coatings of more affordable transition metals, such as electroless NiP, are studied, but the ICR is too high. There is the possibility of using them as a corrosion protective base coating or as part of composite coatings with additions to decrease the ICR<sup>110,111</sup>. These more cost-effective coatings could, furthermore, be utilised for other components in the stack, such as the current collector plates. There is also ongoing research to find high-entropy alloys that

have superior properties to conventional alloys<sup>112,113</sup>. In the high-entropy alloys, close to equimolar composition of several elements are achieved by non-equilibrium synthesis methods, such as PVD and additive manufacturing<sup>114</sup>. These alloys are stabilised by the high entropy, hence the name.

There are some polymer-based coatings<sup>115,116</sup>. However, ICR is often an issue also here. Additions of high amounts of carbon and other conductive particles may mitigate the high ICR of the polymer-based coating, forming a composite coating<sup>117,118</sup>. Mine et al.<sup>119</sup> have proposed screen printing of a carbon composite coating as a cost-effective coating alternative and show that the technique can both reduce the ICR of stainless steel and improve the PEMFC performance as compared to the bare 304. Texturing the coating is suggested to further improve ICR<sup>119</sup>. Such non-vacuum techniques may greatly reduce the manufacturing cost of bipolar plates. However, if coated after forming, the flow field will likely not be coated. Ceramic coatings are, however, the most researched alternative.

The ceramic coatings are most often deposited by PVD. Only a couple hundred nanometres can be enough to protect the substrate. The main drawback of PVD coatings is that the deposition requires a vacuum. PVD coatings such as TiC<sup>120–122</sup>, TiN<sup>115,120,123–125</sup>, CrC<sup>126</sup> and CrN<sup>127–129</sup> have been studied extensively in the literature<sup>26</sup>. Carbon coatings, also mainly produced by PVD, are widely used due to the low ICR towards the GDL, which is also made of carbon, as well as for the chemical stability of carbon in the PEMFC environment. Toyota has exchanged the Pt-coated stainless steel bipolar plates with carbon-coated Ti<sup>8</sup>. The switch from Pt to C for the coating gave sufficient cost reduction to justify the need for a more corrosion-resistant Ti substrate. Recently, amorphous carbon with a Ti or TiC interlayer on a stainless steel substrate has become a promising coating for PEMFCs as it is chemically stable and has low contact resistance to carbon-based GDLs<sup>130–132</sup>.

## 2.5. Bipolar plate production

As mentioned, the bipolar plate has a flow field to evenly distribute the gases over the active area and remove produced water<sup>25</sup>. Inside the bipolar plate, cooling water is circulated to remove produced heat<sup>90</sup>. To make both the flow

field and cooling channels in the metallic bipolar plates, two half plates are stamped or hydroformed. The edges and holes for gas and cooling liquid manifolds are cut by laser to achieve high precision. Finally, the two half plates are welded together to seal the gas and cooling channels. Figure 7 illustrates the manufacturing process.



*Figure 7: The manufacturing process of PEMFC bipolar plates*

The coating can be applied either at the beginning or the end of the production process<sup>90</sup>. While it is more cost-effective to coat the sheet metal before it is formed and cut, it is crucial that all of the following processes are optimised to avoid any defects in the coating. Novalin et al.<sup>133</sup> found oxidised metal particles on top of the coating after the laser cutting that subsequently dissolved during PEMFC operation. Müller et al.<sup>134</sup> studied the effect of pre- and post-coating of C/Cr on 316L and found that no measurable difference in performance or degradation could be found for a 300 cm<sup>2</sup> PEMFC after start-up/shut-down cycling, despite the Cr interlayer being exposed in certain sites for the pre-coated. However, the ICR increased in areas where water is likely to accumulate<sup>134</sup>.

Dependent on the size of the bipolar plate and the conductivity of the back side of the half-plates, welds in the active area might be added to ensure low electrical resistance through the bipolar plate<sup>135</sup>. To reduce the risk of corrosion and to accommodate for the minute geometry of bipolar plates, the joining technique must have minimal width. Therefore, laser welding is a common joining process. Laser welding can be performed autogenously, i.e., no material is added in the joining process. It has been proven that the austenitic structure of SS316 is kept after laser welding<sup>136</sup> and that by adding N<sub>2</sub> to the shielding gas, corrosion around the weld can be minimised<sup>137</sup>.

## 2.6. Interfacial electrical contact resistance measurements

As mentioned in section 1.1.2, the ICR is one of the key parameters for bipolar plate materials. The ICR is a combination of film resistance and constriction resistance<sup>138</sup>. The film resistance originates from the surface oxides of the two contacting surfaces and any contaminations that have adhered to the two surfaces. The constriction resistance originates from the contact not consisting of two smooth surfaces. Thus, instead of the current passing evenly over the whole surface, it is constricted to a limited number of points where the two rough surfaces touch, as shown in Figure 8a. When a force is applied over a surface, the contact points will deform (Figure 8b). This may be both plastic and elastic deformation, and the contact area of each point will increase. Thus, the ICR will decrease (Figure 8c).

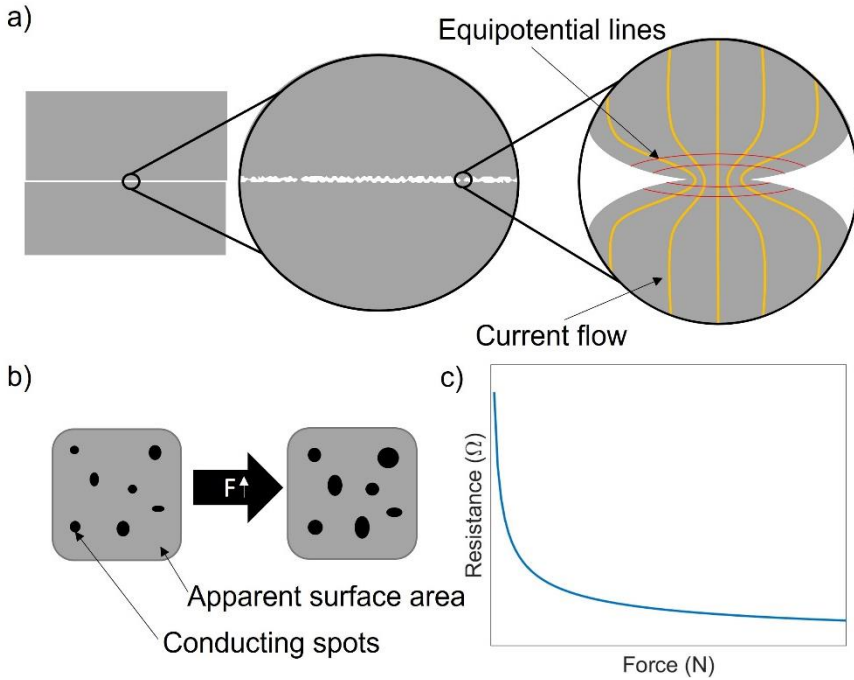


**Figure 8:** a) Illustration of the origin of the constriction resistance, based on Holm<sup>138</sup>, b) the effect of force on the contact area, and c) the change in contact resistance as a function of force.

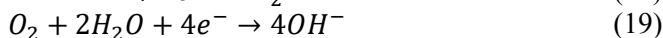
In the PEMFC, the bipolar plate is in contact with the porous GDL. The ICR of the materials for bipolar plates are therefore characterised towards the backing layer of the GDL. Davies et al.<sup>106</sup> first proposed a measurement method where two GDLs were put in between two metallic plates. The sandwich was pressed between two copper probes. The contact resistance was determined by a four-point measurement on the probe. In the four-point resistance measurement, the current is applied between two points and the potential is measured between two separate points. In this way, the resistance of the cables is not influencing the measurement as no current passes through the measurement cables. The method was later adapted by Wang et al.<sup>98</sup> and Kumar et al.<sup>109</sup> to have one metallic sample sandwiched between two GDLs. This setup has been widely adopted for ICR measurements between coated metal plates and GDLs. Several papers have been published on in-situ measurements of the bipolar plate-GDL ICR, showing good agreement with the ex-situ results<sup>35,139,140</sup>. However, Leng et al.<sup>107</sup> compiled an overview of ICR results from different groups and found that there is a lack of consistency in the results between different set-ups.

## 2.7. Corrosion

While the anode and cathode in the PEMFC are well defined and separated by a membrane, the anode and cathode reactions on a corroding surface may occur all over. A site that is anodic at one time may later be cathodic. This is called a mixed electrode and will lead to the whole surface corroding evenly, called general corrosion. The anodic reaction, which is the oxidation of the metal, can, in a general way, be written as:



While the cathodic reaction in an aqueous solution is, in general, either the hydrogen evolution reaction or the oxygen reduction reaction:



To characterise corrosion phenomena, potentiodynamic polarization curves of current versus potential are often obtained (Figure 9). In these curves, the potential is swept, and the resulting current is measured. At low potentials, it

is the cathodic reaction that is dominating, and the current is negative. It is, however, common to plot the logarithm of the absolute value of the current. When the potential is increased, the current will converge towards zero before increasing again. The potential at which the current converges towards zero is when the anodic and cathodic partial currents are equal. Hence, no overall current can be measured. It is also this potential the system will stabilise at when measured at open circuit, and it is then referred to as the open circuit potential (OCP) or the corrosion potential. As the potential increases, the anodic reaction becomes dominating, and the current is positive. In the regions where either the cathodic or anodic currents are dominating, the Tafel equation (equation 9) can be utilised to fit the curves, as long as the currents are sufficiently small that mass transport and ohmic limitations are not coming into play. This is, however, only valid as long as only one reaction is rate-determining. As is shown in Figure 9, the intercept of the Tafel lines of the anodic and cathodic reactions can be utilised to accurately determine the corrosion potential and current.

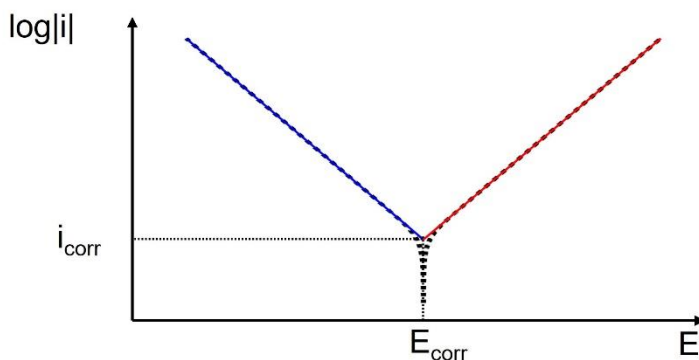


*Figure 9: The cathodic (blue) and anodic (red) Tafel lines, with the intercept marking the corrosion current,  $i_{\text{corr}}$ , and corrosion potential,  $E_{\text{corr}}$ . The dotted line is the sum of anodic and cathodic contributions.*

While the ionic conduction in the electrolyte is not a limiting factor for the anodic reaction, some metals form a stable oxide when oxidised. While there may be an initial peak in current after passing the corrosion potential, the formation of the stable oxide on the metal surface will limit the further oxidation of the metal, and the current will be close to constant at what is

defined as the passive current density (Figure 10). As is seen in the Pourbaix diagrams (Figure 6) for Ta, the passive oxide is stable even at high potentials. For other metals, such as Cr, the stable  $\text{Cr}_2\text{O}_3$  is only stable within a certain potential region, above which the metal is further oxidised and forms soluble ions. In a potentiodynamic polarization curve, this can be observed as a transpassive behaviour, where the current again increases.

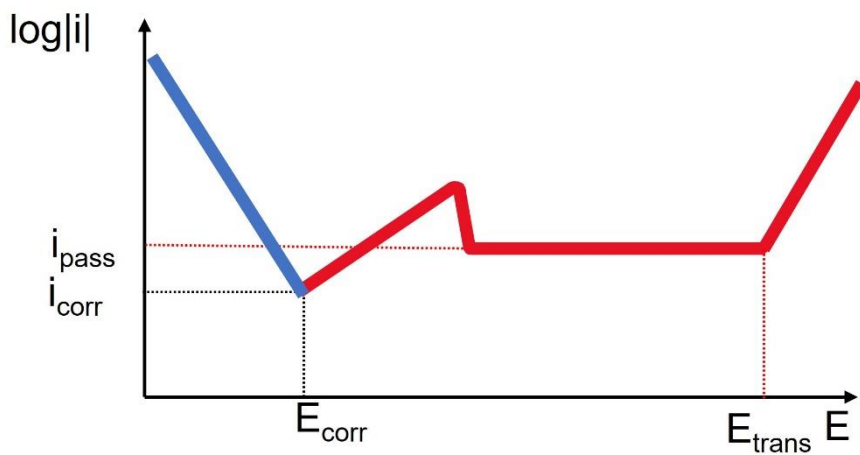


*Figure 10: Schematic of a potentiodynamic polarization curve of a passive material, where the anodic branch (red) has an active peak after  $E_{\text{corr}}$  before stabilising at  $i_{\text{pass}}$ . Finally, after  $E_{\text{trans}}$ , the current again increases.*

In addition to general corrosion, there are several types of localised corrosion, such as galvanic corrosion, crevice corrosion and pitting corrosion. Galvanic corrosion can be found both in general and localised attacks. It is caused by a difference in potential between two materials in contact. An example can be a screw of a less noble quality than the material it was screwed into, where the screw will corrode. For galvanic corrosion to occur, there must be both electrical and ionic contact between the surfaces of the two materials. Correct design and choice of materials can prevent these types of corrosion. Examples of material characteristics or defects on a small scale that causes micro-galvanic coupling can be a local change in alloy composition after welding or defects such as pinholes and cracks in a protective coating.

Crevice corrosion is a local corrosion phenomenon occurring in narrow crevices, such as between two metal plates pressed together or beneath a gasket. The criterium for crevice corrosion is that the supply of oxygen in the liquid phase filling the crevice is controlled by diffusion. The ORR (reaction 19) will be suppressed. Thus, only the anodic reaction will take place in the crevice. The area around the crevice will have an increased current for the cathodic ORR reaction (Figure 11). As there is no  $\text{OH}^-$  production in the crevice, the pH in the crevice will decrease and further destabilise the metal<sup>95</sup>. Crevice corrosion may occur during analysis in an electrochemical cell, as some electrolyte can penetrate into the crevice between the gasket and the sample.

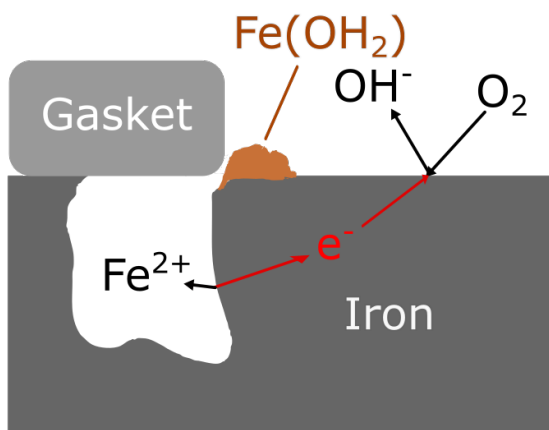


*Figure 11: A schematic illustration of the differential aeration corrosion process in a crevice under a gasket.*

Pitting corrosion occurs on passive materials at local defects in the passive film. It is commonly seen after the material has been exposed to a halide-containing environment and is more severe at higher temperatures. The driving force for the pit is initially that the defected area is less noble than the main material. Hence a micro-galvanic coupling is formed, with a small anodic area and a large surrounding cathodic area. When the pit has formed, it will develop much like a crevice as there is limited diffusion of oxygen into the pit, causing the pH in the pit to be reduced<sup>95</sup>. For stainless steel in the PEMFC environment, the presence of fluoride ions, in combination with the elevated temperature, leaves the material sensitive to pitting corrosion. It is

for this reason that 316L is the most utilised stainless steel for PEMFC application, as the Mo addition, as well as the low carbon content, contributes to lowering the sensitivity of the material towards pit formation.

## 2.8. Ex-situ corrosion testing

When researching new materials for PEMFC components, it is desirable to test the durability early in the development process. The materials are, therefore, performance and durability tested as flat coupons in the size of a few square centimetres. Later, conclusions from ex-situ testing are confirmed by in-situ measurements (Figure 12).

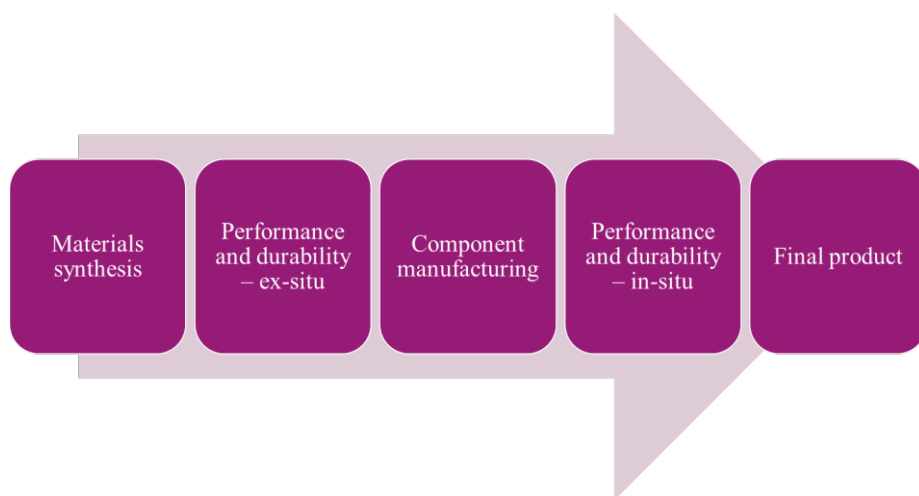


*Figure 12: The development process for new materials for the PEMFC.*

### Electrochemical cell

The stability test for both the catalyst and the bipolar plate materials is done in a three-electrode electrochemical cell (Figure 13). The tested material is connected as the working electrode, the opposite half-reaction in the electrochemical cell occurs on the counter electrode, and the potential of the working electrode is monitored by the reference electrode, as described in section 2.1. All three electrodes are submerged in a liquid electrolyte.

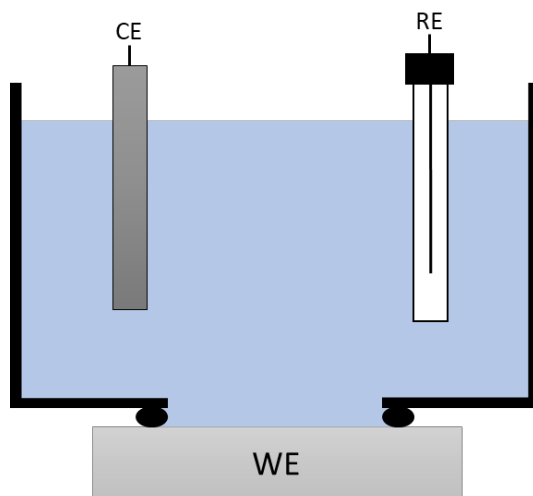


*Figure 13: A three-electrode electrochemical cell, here shown for metallic samples mounted with gaskets towards a hole in the bottom of the cell.*

For the catalyst layer, both performance and durability are commonly tested in 0.1 M  $\text{HClO}_4$ . The potential is cycled between 0.6 and 1.0 V vs RHE to oxidise and reduce the Pt repeatedly. Everything from 1000 to 30 000 cycles is reported in the literature, with 10 000 being the most common, see paper 1. Some report durability in 0.5 M  $\text{H}_2\text{SO}_4$  instead, an electrolyte closer to PFSA, even if it is liquid. The reason many avoid  $\text{H}_2\text{SO}_4$  is sulfate adsorption on the surface of the Pt, reducing performance. No fluorides are added, although membrane degradation releases fluoride ions. To study the stability of the carbon support, the potential is increased to cycle between 1-1.5 V vs RHE, which will oxidise the carbon and simulates the potentials that can be measured during the start-up and shutdown of the PEMFC<sup>141</sup>.

The bipolar plate is located further away from the membrane than the catalyst layer. Since it is difficult to probe the local potential and pH of an operating PEMFC close to the bipolar plate, the materials for the bipolar plate were for a long time tested in the same conditions as the catalyst layer; low pH and potentials up to 1.5 V vs RHE. However, new research utilising in-situ measurements has proven that the potentials at the bipolar plates are 0 V vs RHE at the anode and 0.6 V vs RHE at the cathode, independent of the

potential at the catalyst<sup>29,142</sup>. This is due to the lack of ionic transport between the catalyst layer and the bipolar plate. Furthermore, it is assumed that the pH of the bipolar plate is closer to that of the effluent water, which has been measured to a pH of 3-7<sup>29,92</sup>. The electrolyte commonly used is H<sub>2</sub>SO<sub>4</sub> at 1mM (pH 2.7) or at pH 3, with the addition of 2 ppm F<sup>-</sup>. Lædre et al.<sup>103</sup> studied the effect of electrolyte pH and halide addition on the potentiodynamic polarization curve of stainless steel. The addition of halides, either 2 ppm F<sup>-</sup> or 10 ppm Cl<sup>-</sup> did not influence the corrosion due to the small amounts added. However, they found a significant difference between the more realistic 1 mM H<sub>2</sub>SO<sub>4</sub> to the aggressive 1 M H<sub>2</sub>SO<sub>4</sub><sup>103</sup>, as was also found by Feng et al.<sup>104</sup>.

In the standard electrochemical cell, the average corrosion over the exposed area is measured. The only way to differentiate between general and localised corrosion phenomena is to study the samples in a microscope after exposure. To avoid crevice corrosion due to the measurement setup, an Avesta cell may be used (Figure 14a). In the Avesta cell, a small flow of distilled water is pumped beneath the gasket to ensure that there is no stagnant electrolyte with a subsequent build-up of ions beneath the gasket<sup>143</sup>.

To characterise local corrosion phenomena, part of or the whole electrochemical cell must be miniaturised. One way is to expose only a small area of the sample to the electrolyte by utilising a capillary (Figure 14b). This is called an electrochemical micro-cell<sup>144</sup>. The capillary can be as small as 50 µm in diameter. Thus, different microstructural features can be studied for coarse-grained structures. The only requirement is that the studied surface area is completely flat so that no electrolyte leaks out. Alternatively, a method with a gap between the capillary and the sample surface can be used. This is often referred to as the droplet method, as the gap should be of a size such that a droplet is stabilised between the capillary and the surface, and the surface tension ensures that there is no leakage. The disadvantage is that the examined area becomes less well-defined and might change during measurement due to evaporation.

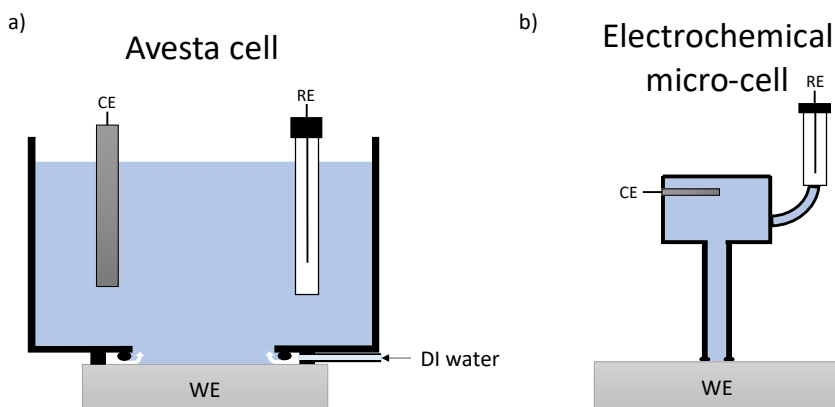


*Figure 14: Schematic illustration of a) an Avesta cell and b) an electrochemical micro-cell. Notice that the images are not to scale.*

## Environmental durability testing

The electrochemical cell tests the stability of materials and coatings in immersion, but environmental durability tests are also needed. One way to do this is through field testing, where the samples are exposed to an environment of choice and left for a certain amount of time<sup>95</sup>. Examples are test reference centres where samples are exposed to local weather conditions. However, a test typically takes several years. Similarly, samples can be mounted on trucks to simulate the corrosion of vehicle components<sup>95</sup>. For the PEMFC, this kind of exposure requires the fabrication of a full stack and operation of the PEMFC in a relevant way, either as a stationary or vehicle system. Hu et al.<sup>46</sup> recently published results for catalyst degradation from a PEMFC after one year in a vehicle with a total operation time of 1800 hours. However, when screening new materials, a shorter test duration is needed. This is where the accelerated test methods come in. Commonly either climate, corrosive gas or salt spray is used in the accelerated test or a combination of the three. In the climate test, temperature and humidity are cycled together so that the surface goes through accelerated condensation and drying cycles. UV light may be added, especially for organic coatings<sup>95</sup>. There are multiple different standards, differing in the maximum and minimum temperatures and humidity and cycle length<sup>95,145</sup>. In the corrosive gas test, corrosive species found in a traffic or industrial environment are vented in the test chamber at a higher rate

and concentration. SO<sub>2</sub> and NO<sub>2</sub> are added to represent exhaust from fossil fuels found in traffic environments. H<sub>2</sub>S and Cl<sub>2</sub> are found close to certain industries<sup>146</sup>. In the salt spray test, a salt solution is sprayed onto the sample. There are several different standards specifying if the salt spray should be neutral or acetic and if it is a constant spray or cyclic, where the salts are allowed to dry on the surface<sup>95</sup>. When it comes to environmental testing of materials for the PEMFC bipolar plate, the temperature, humidity, and possible air filtering means that these standards are not directly applicable.

## 2.9. In-situ accelerated stress testing

A compromise between ex-situ testing and field-testing components in a full-size PEMFC used in a real application is to do accelerated stress tests (ASTs) in the PEMFC. There are several ASTs focusing on the conditions for the degradation of specific components. For example, the US DOE has formulated a catalyst AST cycling the cell voltage between 0.6-1.0 V, while the catalyst support AST requires cycling between 1.0-1.5 V<sup>141</sup>. The membrane is most sensitive to degradation at OCV, which in combination with relative humidity cycling to induce mechanical stress, is part of the membrane AST<sup>141</sup>. No specific AST exists for the bipolar plate. Another approach is to stress the cell by deviating from normal operating conditions, as formulated in the test protocol for single cells by the European Joint Research Centre for Fuel Cells<sup>147</sup>. Within the literature on the synthesis and testing of new materials for PEMFCs, the majority of the in-situ measurements are performed in single cells. Graphite flow plates are used for catalyst and membrane experiments to increase the durability of the cell house and avoid degradation due to metal flow plate corrosion. There is ongoing research to construct single cells that have minimal influence on the test results to be used as a reference, for example, the zero-gradient cell developed by the European Joint Research Centre<sup>148,149</sup>.

Furthermore, accelerated load cycles exist, which instead of accelerating a specific degradation mechanism, compress all different operating conditions that can be found during normal operation into a shorter time span<sup>150</sup>. In its simplest form, in the case of automotive PEMFCs, data from vehicle drive cycles given in km/h is converted to a percentage of maximum load<sup>147,151</sup>. The

conversion is not entirely straightforward as all fuel cell electric vehicles have a battery, and dependent on the sizing of the battery and the fuel cell, the load cycle of the fuel cell will vary. In addition to the load cycle, several other variables should be considered when constructing a reliable accelerated stress test. Among these are temperature and humidity, which may vary during the load cycle<sup>152</sup>. The start-up and shutdown of the PEMFC should also be controlled<sup>153,154</sup>, and there is often a difference in how a shorter stop will affect the cell as compared to a longer stop. To take all variables into account, freeze cycles to simulate a vehicle during a long stop in winter conditions should be added<sup>155</sup>. There is still work to be done to validate and standardise these types of tests.

### 3. Research methodology

Based on the four research questions defined in section 1.3, six works were performed, each resulting in a paper. Papers 1 and 2 are related to RQ1 on the catalyst material. Paper 1 is a literature study on the recent developments in cathode catalyst materials, and Paper 2 focuses on electrodeposition of PtNi and PtNiMo particles. Paper 3 and 4 relates to RQ2 on the measurement methodology for interfacial contact resistance, while papers 5 and 6 are related to localised corrosion on bipolar plates. RQ4 on PEMFC testing is touched upon in both papers 2 and 5. Figure 15 illustrates the focus of each performed work put into the materials testing process context.

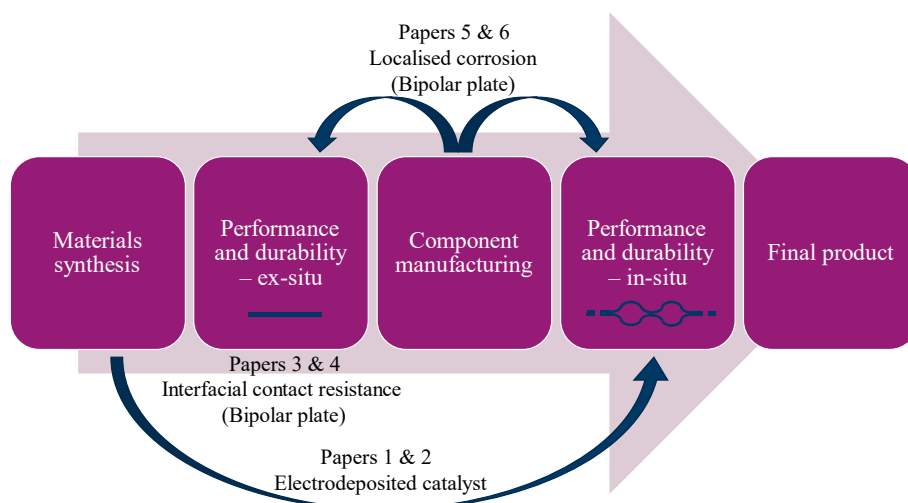


*Figure 15: The focus of the performed work, put into the context of the development process of new materials for the PEMFC.*

#### 3.1. Materials

For paper 2, the synthesis of the catalyst nanoparticles by electrodeposition is described in section 0, and the fuel cell set-up is described in section 3.3.

For paper 3, aluminium AA1050 was ordered and coated first with electroless NiP with a high P content (10-13 wt%), and half of the samples furthermore got a top coating of electrodeposited NiSn. The material selection was based on the requirements of the current collector plate, which needs low ICR both towards the GDL and towards metal components in the power terminal. Six additional samples with NiP were coated with electrodeposited Au to be used as reference material during the contact resistance measurements. All coatings were plated by the commercially available processes at LPTech AB.

For paper 4, stainless steel 316L was chosen as a substrate since the PEMFC and PEM water electrolyser bipolar plate was the intended application areas. The coating was a CrFeNi alloy with varying amounts of Ta and W to improve passivation. The coating was applied by PVD at Uppsala University using one target of equimolar CrFeNi and one target with either Ta or W. The coatings were first applied on SiO<sub>2</sub> wafers to study the corrosion resistance without interference from the substrate. A second set of samples were coated on the stainless steel 316L for the ICR measurements.

The flow plates for the PEMFC used in papers 2 and 5 were made of stainless steel 316L with a Sandvik Sanergy LT coating. The coated metal sheet was hydroformed and laser cut by Borit NV (Figure 16). No adjustments to the plate geometry were done to accommodate the precoated material. Flat samples of the coated material and uncoated stainless steel flow plates were also acquired.

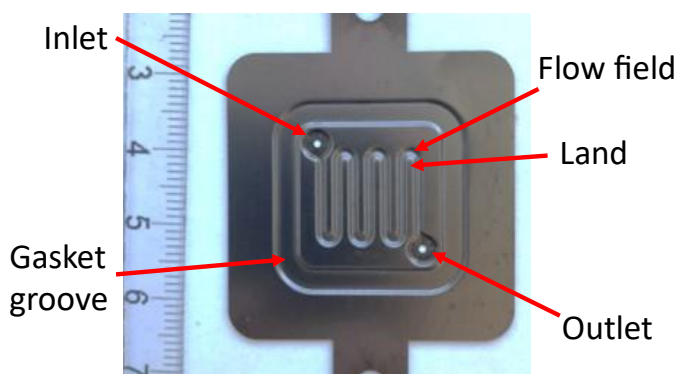


*Figure 16: The hydroformed flow plate utilised in papers 2 and 5. The scale is in cm.*

For paper 6, one flat and one adiabatically stamped plate of stainless steel 304, both of thickness 0.1 mm, were studied. Holes were laser cut, and the two plates were welded together by an IPG 1000 W fibre laser with Ar as shielding gas and N<sub>2</sub> as root gas. The sample preparation was performed at a commercial facility.

## 3.2. Electrochemical experiments

Electrochemical cells have been used for electrodeposition, performance, and corrosion testing. In all cases, Pt has been used as a counter electrode and Ag/AgCl in a 3 M KCl solution has been used as a reference electrode unless stated otherwise.

### Electrodeposition

Electrodeposition of PtNi and PtNiMo nanoparticles was performed in an electrochemical cell. The Freudenberg GDL was taped with Kapton tape onto a copper plate to form the working electrode. After some optimisation of the deposition parameters to achieve the desired composition with as small a particle size as possible, a pulsed current electrodeposition process was decided upon. It was found that a stabiliser in the form of citric acid was needed upon adding Mo to the electrolyte to increase the Mo content by complexing. All process parameters are given in Paper 2.

### Catalytic performance

The electrodeposited catalyst was first activated by cycling the potential, and the activity was measured by cyclic voltammograms (CV) and linear sweep in 0.5 M H<sub>2</sub>SO<sub>4</sub>. To be comparable to the literature results, the experiment was repeated for some samples in 0.1 M HClO<sub>4</sub>.

### Corrosion

Both potentiostatic and potentiodynamic polarization has been performed to study the stability of coated metallic samples in an electrolyte to simulate the PEMFC environment. Prior to the potentiodynamic polarization curves, the OCP was measured. The duration of the OCP measurement depended on the sample and how long it took to reach a stable OCP. The potentiodynamic

polarization has been carried out from 50 mV below the OCP to 1 V vs Ag/AgCl or higher. Potentiostatic polarization was performed at 0.6 and 1.5 V vs Ag/AgCl to simulate the PEMFC and the PEM water electrolyser, respectively. All experiments have been performed at room temperature.

For paper 4, both potentiodynamic and potentiostatic polarization was performed in 0.05 M H<sub>2</sub>SO<sub>4</sub>.

For paper 5, 0.5 M H<sub>2</sub>SO<sub>4</sub> was utilised as an electrolyte in both the standard electrochemical cell and the electrochemical micro-cell (Figure 17). The electrochemical cell for the flow plate was designed to fit the gasket groove of the flow plate. The electrochemical microcell was mounted with a glass capillary of 800  $\mu$ m in diameter. The capillary was dipped in silicone to form the gasket. A Luggin capillary was utilised to connect to the Ag/AgCl reference electrode.

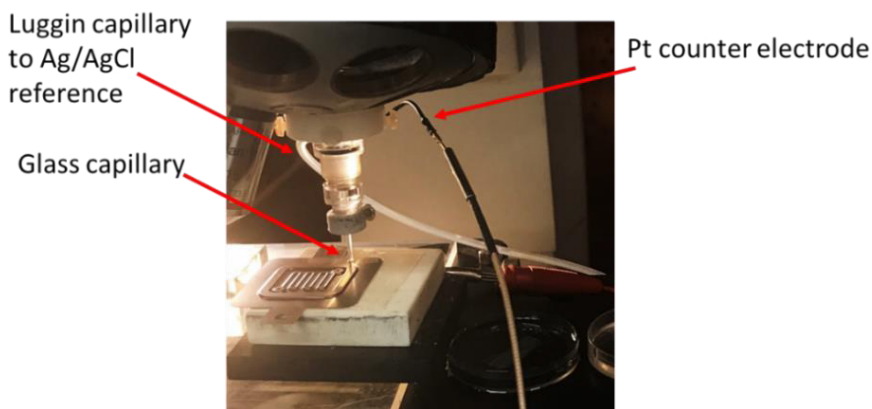


*Figure 17: The electrochemical micro-cell utilised, when measuring on a flow plate.*

For paper 6, where bare stainless steel was studied to see the corrosion resistance of the weld, an Avesta cell was utilised to avoid crevice corrosion under the gasket. The electrolyte was 1 mM H<sub>2</sub>SO<sub>4</sub> with 2 ppm of fluoride added as NaF, and N<sub>2</sub> was bubbled through the electrolyte to remove dissolved O<sub>2</sub>. A summary of the experiments performed in electrochemical cells can be found in Table 2.

**Table 2: The details for all experiments performed in electrochemical cells.**

<b>Analysis</b>	<b>Paper</b>	<b>Sample</b>	<b>Electrolyte</b>	<b>Area</b>
Electrodeposition	2	GDL	Metal salts	4 cm <sup>2</sup>
Catalyst activity	2	GDE	0.5 M H <sub>2</sub> SO <sub>4</sub>	4 cm <sup>2</sup>
Catalyst activity	2	GDE	0.1 M HClO <sub>4</sub>	4 cm <sup>2</sup>
Potentiodynamic	4	CrFeNiTa/W	0.05 M H <sub>2</sub> SO <sub>4</sub>	4 cm <sup>2</sup>
Potentiostatic	4	CrFeNiTa	0.05 M H <sub>2</sub> SO <sub>4</sub>	4 cm <sup>2</sup>
Potentiodynamic	5	C/Ti/SS316L	0.5 M H <sub>2</sub> SO <sub>4</sub>	1.1/ 3 cm <sup>2</sup>
Potentiodynamic micro-cell	5	C/Ti/SS316L	0.5 M H <sub>2</sub> SO <sub>4</sub>	0.5 mm <sup>2</sup>
Potentiodynamic Avesta cell	6	SS304	1 mM H <sub>2</sub> SO <sub>4</sub> + 2ppm F <sup>-</sup>	1 cm <sup>2</sup>

### 3.3. PEMFC single cell

A PEMFC single cell with metallic flow plates was used for the PEMFC experiments (Figure 18). The flow plates were described in section 3.1. The active area of the flow plates was 2.9 cm<sup>2</sup>.

GDEs with 0.3 mg<sub>Pt</sub>/cm<sup>2</sup> from Fuel Cell Store were used on both the anode and cathode. In Paper 2, the cathode GDE is exchanged for Freudenberg GDL with PtNi and PtNiMo nanoparticles electrodeposited on the MPL. A Nafion 212 membrane was utilised in all experiments. To ensure proton conduction when operating with the electrodeposited catalyst, the GDEs were hot pressed at 110°C and 5 bar pressure to form the MEA. The Nafion 212 membrane and commercial GDE were purchased in a batch at the beginning of the work, and the same batch has been utilised across the different papers.

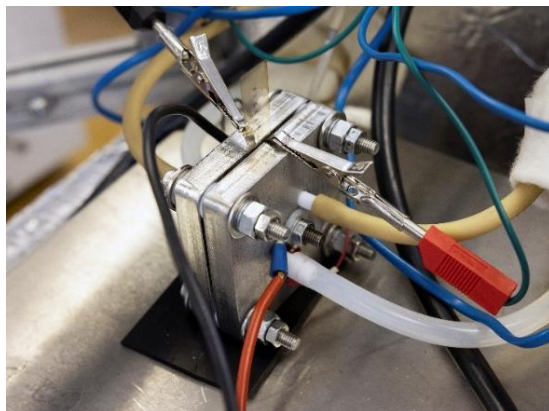


*Figure 18: The PEMFC single cell utilised, mounted in the test station. Connected at gas inlet and outlet, and with electrical wires.*

The single cell was assembled with the compression ensured by four screws, and the cell was tested in a Greenlight Innovation Inc. G20 test station with a built-in load bank and potentiostat. The inlet gas temperature was set to  $80 \pm 5^\circ\text{C}$  and the dew point to  $65 \pm 1^\circ\text{C}$ , giving a relative humidity (RH) of  $52 \pm 10\%$  unless stated otherwise.

In paper 2, the PEMFC was potentiostatically cycled between 0.6 and 0.9 V with a cycle time of 16 seconds, deviating from the standard catalyst cycle in the maximum potential as it was observed that the cells with the electrodeposited catalyst could not reach 1 V.

In paper 5, the effect of load cycle and relative humidity was studied. Three different load cycles were applied, all with the same average current density. One held a constant current, the second had a square wave, and the third had a triangle wave. The cycle time for the triangle and the square was the same. The cells were shut down and restarted once a week. Lastly, the triangle wave cycle was repeated at a higher relative humidity of 80%. The total test duration for the tests was 500 hours.

### 3.4. Interfacial electrical contact resistance measurements

ICR measurements were performed in the test rig shown in Figure 19. The probes are made of brass with a gold coating on the contacting surface. An Agilent 34420A resistance meter measured the resistance, and a scale was used to measure the applied force. All ICR measurements were performed in a room with  $23 \pm 2^\circ\text{C}$  and a humidity of  $14 \pm 3\%\text{RH}$ .

A Freudenberg H23 carbon paper that has no PTFE treatment and no MPL was used for ICR measurements.

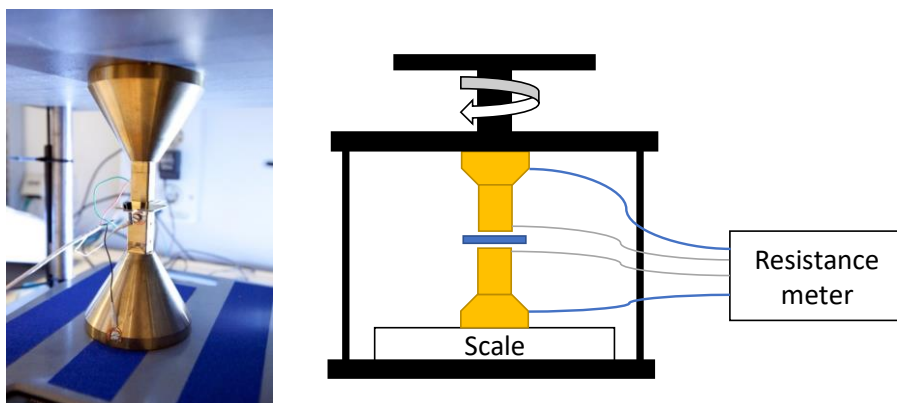


*Figure 19: The test rig for ICR measurements*

### 3.5. Environmental durability

The NiP and NiSn on Al were tested in a climate chamber and by mixed gases. Both tests were chosen from the IEC 60068-2 standard<sup>145,146</sup>. The climate cycle in IEC 60068-2-38 was adapted to PEMFC applications by increasing the maximum temperature to  $85^\circ\text{C}$  to match the operating temperature of the PEMFC while keeping the  $-10^\circ\text{C}$  minimum temperature. A total test duration of 10 days was chosen.

Method 4 for mixed gas cycling was chosen from IEC 60068-2-60 to take into account any possible industrial or traffic environment in which a PEMFC can

be placed, with a duration of 21 days. In the test, the chamber is vented with  $\text{H}_2\text{S}$ ,  $\text{NO}_2$ ,  $\text{Cl}_2$  and  $\text{SO}_2$  at  $25\pm 1^\circ\text{C}$  and  $75\pm 3\%\text{RH}$ .

Both flat samples and a prototype screw connection (Figure 20) were tested in the climate cycle. In contrast, only flat samples were tested in the mixed gas chamber as the prototype test rig was not sufficiently inert to sustain the more aggressive cycle.

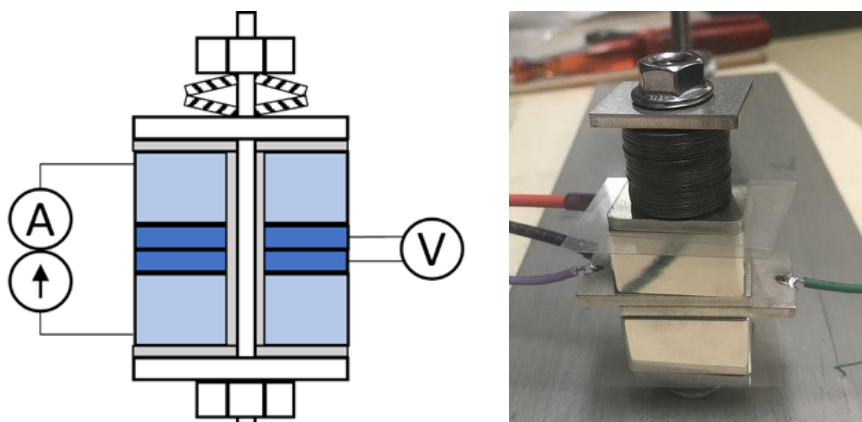


*Figure 20: Schematic illustration and a photograph of the prototype screw connection. The blue squares are NiP or NiSn-coated samples, the grey parts are insulation, the white are stainless steel, and the striped are the disc springs utilised to control the compression.*

### 3.6. Materials characterisation

The materials in the project have been characterised by light optical microscopy (LOM), scanning electron microscopy (SEM) and transmission electron microscopy (TEM), dependent on the size of the studied features in descending order. In the SEM, energy dispersive x-ray spectroscopy (EDS) has been utilised to analyse the chemical composition of the samples. For coated samples, EDS was performed on the cross-section to avoid the influence of the bulk material on the results. Electron backscatter diffraction (EBSD) was utilised to characterise the grain structure and phase composition of the welded stainless steel plates.

For accurate chemical analysis of the electrodeposited nanoparticles, the GDLs with the particles were dissolved in aqua regia, and the solution was analysed by inductively coupled plasma mass spectrometry (ICP-MS). Surface analysis of coated and corroded samples has been performed by x-ray photoelectron spectroscopy (XPS) to analyse the composition of the surface layer only. X-ray diffraction (XRD) is utilised to study the crystal structure.

Which analytical techniques have been applied for which sets of samples are summarised in Table 3.

*Table 3: Overview of the experimental procedure for each set of metallic samples for bipolar plates*

	<b>PtNi/ PtNiMo</b>	<b>NiP/NiSn on Al</b>	<b>CFNT on SS316L</b>	<b>Precoated SS316L</b>	<b>Welded SS304</b>
<i>In paper</i>	2	3	4	5	6
LOM + roughness		X			X
SEM	X	X	X	X	X
TEM	X		X		
XRD	X		X		
XPS	X		X		X
ICR		X	X		
Catalytic activity	X				
Potentiodynamic polarization			X	X	X
Electrochemical micro-cell				X	
Environmental durability		X			
Potentiostatic polarization			X		
In-situ PEMFC	X			X	

## 4. Results and discussion

### 4.1. Electrodeposited Pt-Ni and Pt-Ni-Mo

Electrodeposition as a synthesis method for the PEMFC cathode catalyst facilitates the testing of new alloy compositions in the PEMFC. In paper 2, electrodeposition of Pt-Ni and Pt-Ni-Mo is studied. SEM micrographs show that the produced Pt-Ni particles have an average particle size of ~40 nm with an even particle size distribution, while the Pt-Ni-Mo have a mix of small and large particles, with the smaller in the same range of the Pt-Ni and the larger up to 80 nm. Figure 21 shows a representative selection of the catalysts synthesised. The cross-sectional SEM micrograph shows that the catalyst layer has a thickness of less than 0.5  $\mu\text{m}$  (Figure 22). This shows that even though the whole GDL was immersed in the electrolyte, the hydrophobicity of the MPL, and the directional nature of the electrodeposition process, ensured that the electrodeposition occurred only on the top surface. This facilitates proton conduction to the membrane, and it is therefore chosen not to add ionomer before the PEMFC test. However, it limits the amount of deposited material.

The results from the ICP-MS of fully dissolved GDEs reveal that the composition of the Pt-Ni varies from 20-33% Ni. The Pt-Ni-Mo has a more varied composition, with two samples rich in Pt and low in Mo and two samples more Ni-rich, with moderate Mo content and little Pt. The loading is two orders of magnitude below the commercial reference at 0.9-7.4  $\mu\text{g}/\text{cm}^2$ . The XPS data show that while Pt and Ni are found primarily in their metallic state, Mo is not fully reduced during the electrodeposition. Furthermore, the Pt-Ni-Mo samples have low current efficiency of the electrodeposition process of only 2-12%, compared to 25% for the Pt-Ni.

The CVs of the catalysts in 0.5 M  $\text{H}_2\text{SO}_4$  indicate that the Pt-Ni-Mo samples have a somewhat higher active surface area as compared to the Pt-Ni (Figure 23). It should, however, be considered that the loading varies.

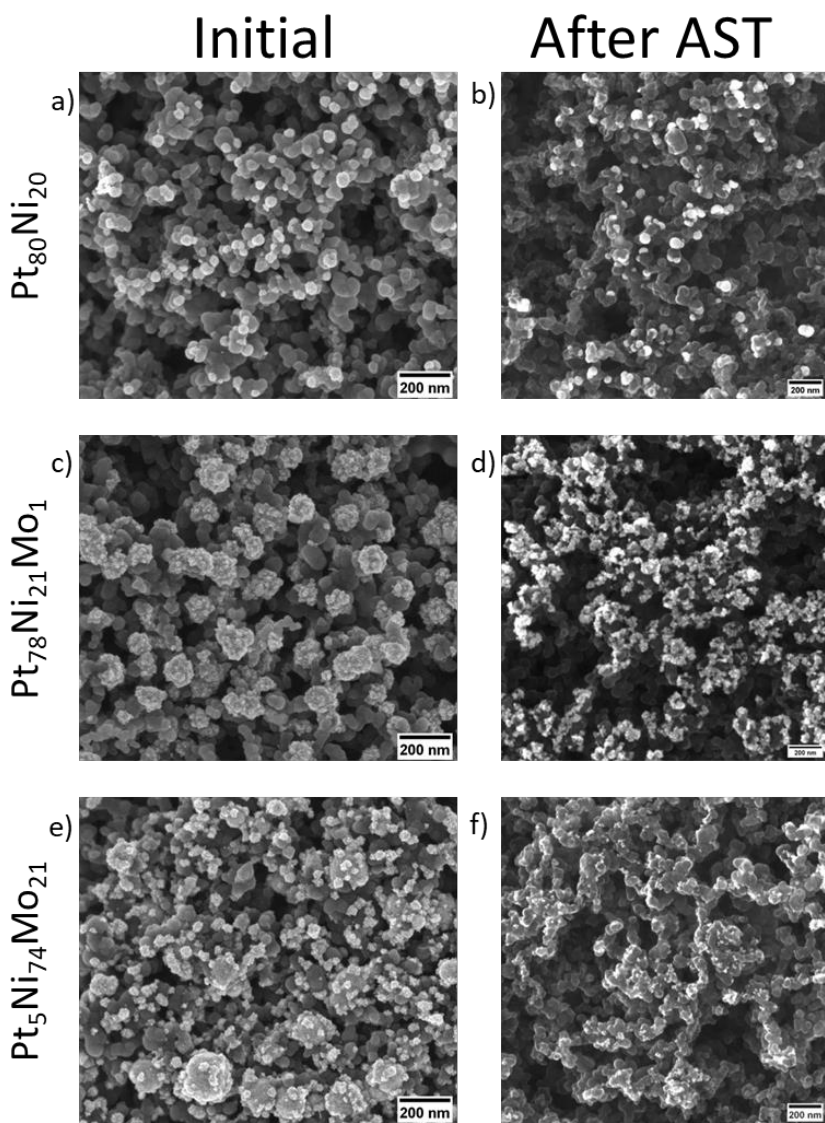


Figure 21: SEM images of three representative samples  $\text{Pt}_{80}\text{Ni}_{20}$  (a and b),  $\text{Pt}_{78}\text{Ni}_{21}\text{Mo}_1$  (c and d), and  $\text{Pt}_5\text{Ni}_{74}\text{Mo}_{21}$  (e and f) both before and after AST.

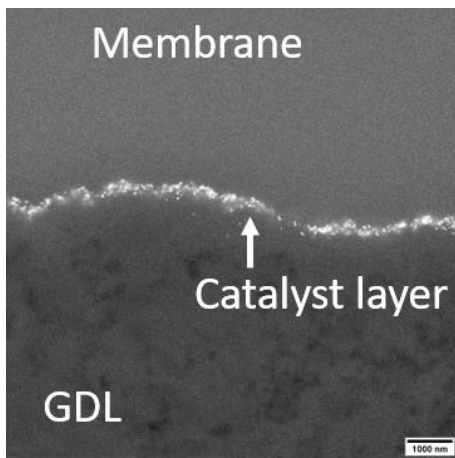


Figure 22: A cross-section of the MEA with the  $Pt_{66}Ni_{32}Mo_1$  catalyst after hot-pressing

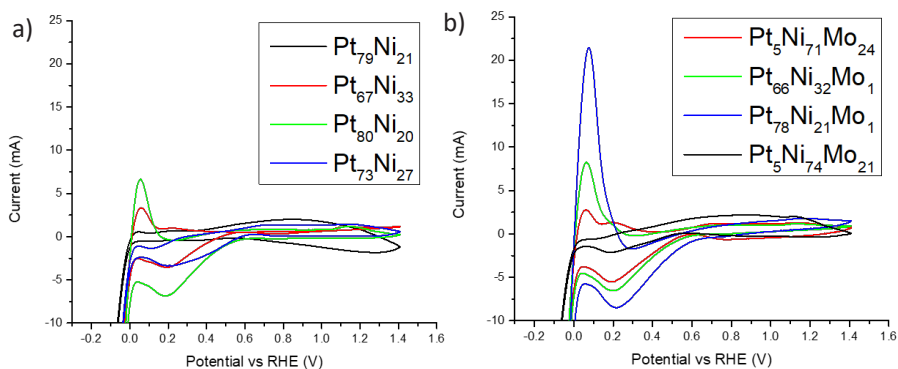
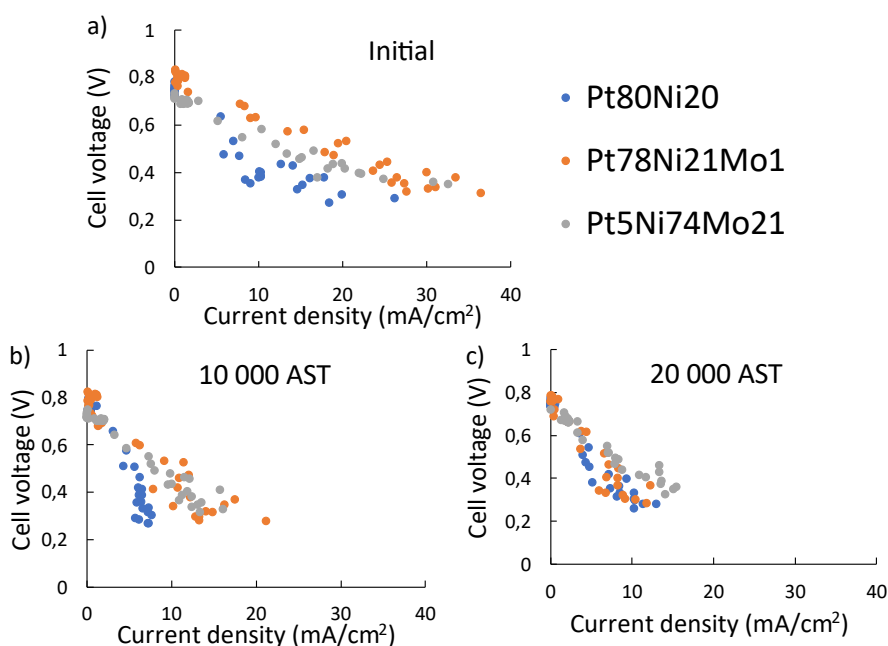


Figure 23: The CVs of the electrodeposited (a) PtNi and (b) PtNiMo catalyst measured in 0.5 M  $H_2SO_4$  at 25°C and a sweep rate of 50 mV/s.

In the in-situ PEMFC tests of the catalysts hot pressed onto a Nafion 212 membrane all samples show similar performance (Figure 24a). Due to the low loading, low current densities are achieved. Still, stable performance allowed

for running 20 000 AST cycles between 0.6 and 0.9 V. The most common AST for the catalyst is cycling between 0.6 and 1.0 V. However, it was observed in the initial testing that none of the cells reached above 0.9 V, so it was decided to limit the AST cycle. Figure 24b shows that there is a significant loss of performance during the first half of the AST. However, the performance stabilised and was almost unchanged for the last half (Figure 24c). The loss in performance is similar for all samples. The results fit well with the literature stating that a larger loss of performance is observed at the beginning of life, as unstable catalyst sites are dissolved. After some time, the particles are more stable. Thus, the performance stabilises.



*Figure 24: The PEMFC polarization curves of a representative selection of the electrodeposited catalyst after activation and after 10 000 and 20 000 AST cycles. Each potential was held for three minutes, averaging the last minute for the measurement.*

SEM images of the particles after the AST show a reduction in the size of the particles as well as a reduced number of particles (Figure 21), although it should be considered that some particles may adhere to the membrane or be

lost during the detachment. The sample with the lowest amount of Pt, Pt<sub>5</sub>Ni<sub>74</sub>Mo<sub>21</sub>, appears to have the greatest loss of catalyst material. Still, the performance in the PEMFC after 20 000 cycles is equal to the other alloys, showing high activity of the particles that are left.

With regards to research question 1, this show that electrodeposition can be utilised for catalyst synthesis and allow a high degree of flexibility in alloy composition also for more complex alloys. The facile synthesis gives the opportunity to quickly screen new catalyst alloy nanoparticles directly in the PEMFC to complement screening in a three-electrode electrochemical cell. However, a reduction in particle size and an increase in loading is needed to be able to compare the performance of the PEMFC to the commercial catalysts available.

With regard to research question 4, the degradation mechanism of the catalyst particles cannot be determined fully from the presented work. What can be said is that with low Pt loading, the particle size reduces significantly, indicating that these alloys are prone to dissolution. The low loading and loss of material during detachment of the GDE from the membrane, unfortunately, hinder further chemical analysis of the catalyst after in-situ testing.

## 4.2. Effect of passivation on the ICR

The measurement of the ICR for PEMFC bipolar plates has been described by several authors in the literature<sup>98,106,109</sup>. However, although the set-up of the measurement is detailed in the literature, the procedure of obtaining the measurement data is not equally well described. The GDL will be both plastically and elastically deformed during the measurement. Over time, there will be some relaxation, so the pressure will decrease. It is, therefore, important that the same procedure is followed regarding the type of GDL and compression of the GDL so that the GDLs used in different measurements are in an equally mechanically deformed state. A procedure for this is the goal of the following work. Furthermore, the developed procedure is utilised to measure the ICR of both aluminium samples with NiP and NiSn coatings and stainless steel 316L with CrFeNi coatings with varying Ta addition. Relevant accelerated ageing tests have been performed for each set of samples, and the effect on the ICR is investigated.

### 4.2.1. *Characterization of the coated samples*

Prior to measuring the ICR, the surfaces of the samples were analysed with respect to surface roughness and chemical composition.

#### NiP and NiSn on aluminium

The coated aluminium substrates in paper 3 were studied first with the digital optical microscope to obtain the surface roughness. Subsequently, cross-sections were cut to study the thickness and composition of the coatings by SEM and EDS. The electroless NiP has a phosphorous content of 11 wt%, thus falling into the category of high P, as intended, and a thickness of 8.8  $\mu\text{m}$ . The electrodeposited NiSn has a Sn content of 72 wt% (56 at%) and a thickness of 2  $\mu\text{m}$ . All samples have a roughness,  $S_q$ , of about 0.9  $\mu\text{m}$ , which is found to originate from cutting or grinding of the substrate prior to the deposition.

#### CrFeNiTa and CrFeNiW on stainless steel

In Paper 4, the effect of Ta and W additions to a CrFeNi coating on the passive behaviour at higher potentials as well as the ICR, is studied. The composition

of the coatings after PVD is determined by XPS. Ta contents of 11, 13, 15 and 25 at% and W contents of 13, 19, 25, 32, 37 and 45 at% are achieved. In addition, a pure CrFeNi coating and pure Ta and W coatings as references have been synthesised. XRD confirms that only the pure CrFeNi sample is crystalline, while all samples with Ta and W additions are amorphous. The thickness determined by SEM is between 430 and 680 nm. From the potentiodynamic measurements of the coatings in 0.05 M H<sub>2</sub>SO<sub>4</sub>, with subsequent XPS and SEM analysis, it is concluded that only the samples with more than 15 at% Ta and the sample with 45 at% W show passive behaviour up to 1.7 V. From XPS analysis it can be seen that Ta is enriched in the oxide layer, much like how Cr is enriched in stainless steels. At the same time, W is instead found evenly in the bulk and oxide. Hence, a smaller amount of Ta is needed to form a continuous Ta-containing oxide layer. Furthermore, the W-rich oxide appears to be nanoporous. Hence, it is less protective than the dense Ta oxide. From this, it has been decided that the Ta samples are the most promising for PEMFC and water electrolyser applications. These coatings have been reproduced on stainless steel 316L for analysis of the ICR in pristine and aged conditions.

#### **4.2.2. *Interfacial contact resistance methodology***

The first step in understanding the ICR measurement for PEMFC bipolar plates is to understand the effect of the chosen GDL on the measurement. To do this, three GDLs were separately and repeatedly compressed between the same two NiP-coated samples to see how the measurements deviated (Figure 25). It can be seen that for each GDL, the first compression gives dissimilar curves. However, the second and third compression is on top of each other. Furthermore, the third measurement for all three GDLs is equal, proving the repeatability of the measurement. The multiple compressions were performed by obtaining the first curve from the lowest to the highest pressure, then going back to the lowest pressure and starting the next curve. The pressure was not entirely released during the measurement to avoid misalignments in the repeated compressions. This shows that there is some variance in the initial response of the GDL, and it is mechanically deformed during the compression. By repeating the compression, the GDLs mechanical deformation is normalised, and all GDLs give equal ICR values.

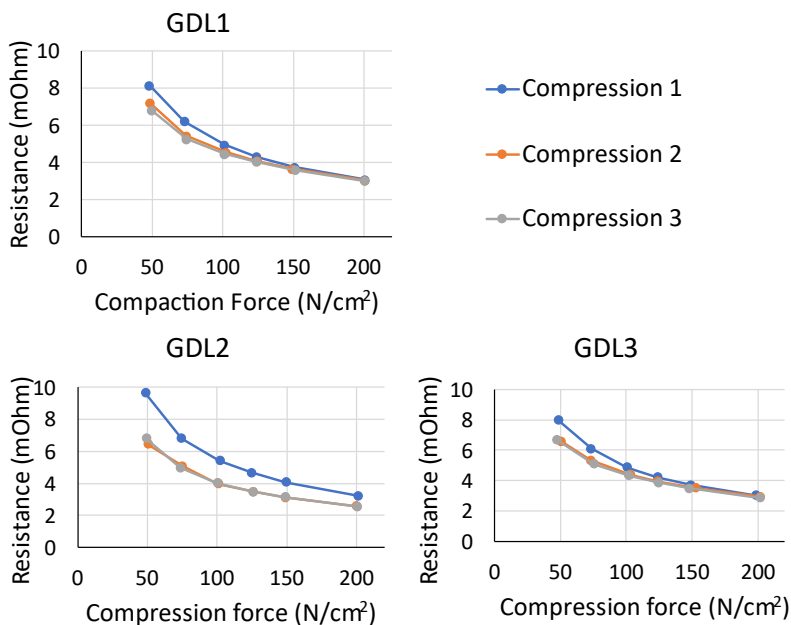


*Figure 25: ICR measurements of the same NiP-coated samples with three different GDLs and three iterations of compression.*

The experiment was repeated for three separate sets of samples for validation. For all samples, the curve for the first compression gives higher resistance and more deviation between the three GDLs. The deviation between the three GDLs is largest at lower compaction force. This concurs with the conclusions for the first set of samples. When comparing the graph for different GDLs (Figure 26a) and the graph for different sets of samples (Figure 26b), it is clear that the standard deviation is larger when comparing different samples. Furthermore, while the deviation between GDLs becomes smaller at higher compression force, the deviation between different samples does not reduce in the same way. It can therefore be concluded that the repeated compressions reduce the measurement uncertainty that originates from the GDL. Furthermore, even though the variance in ICR of the GDL still contributes to the measurement uncertainty, there is also a significant variance between samples. To account for this, multiple samples should always be measured to give reliable conclusions on the ICR of different materials and coatings. In the following work, three sets of samples of each coating are measured.

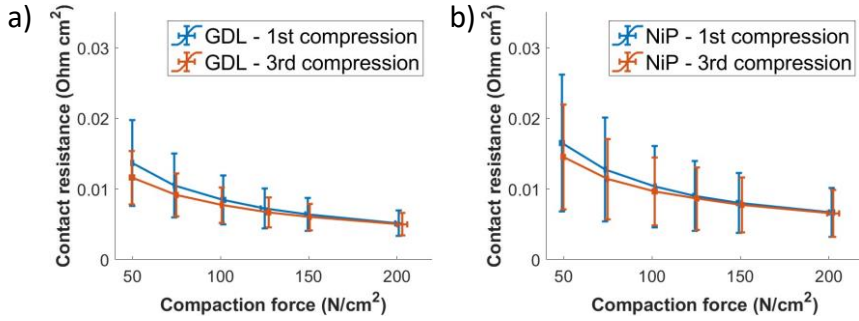


**Figure 26: ICR measurements performed with the proposed method plotted with standard deviations a) from three different GDLs and b) from three different sets of samples.**

The setup for the ICR measurements furthermore deviates from that of Wang et al.<sup>98</sup> and Kumar et al.<sup>109</sup> in that instead of sandwiching a sample between two GDLs, one GDL is sandwiched between two samples (Figure 27). This is done after inspection of the GDL to ensure that the top and bottom of the GDL are similar. A GDL without any PTFE treatment and without an MPL is chosen for these measurements to ensure that the top and bottom have equal resistance. The voltage is measured between the two samples, removing the need for subtracting a measurement of the probe-GDL ICR as is done in the reference method. It furthermore allows for the measurement of samples coated only on one side. Comparative measurements of the reference set-up and the proposed set-up were performed. The reference method requires five consecutive compressions, while the proposed method stabilises after only three. It is therefore concluded that the proposed method shortens the measurement procedure by removing the need to perform a reference measurement of only the GDL, as well as requiring fewer compressions to normalise the GDL mechanically. The proposed method is the method used for all metal-GDL ICR measurements in the following section.

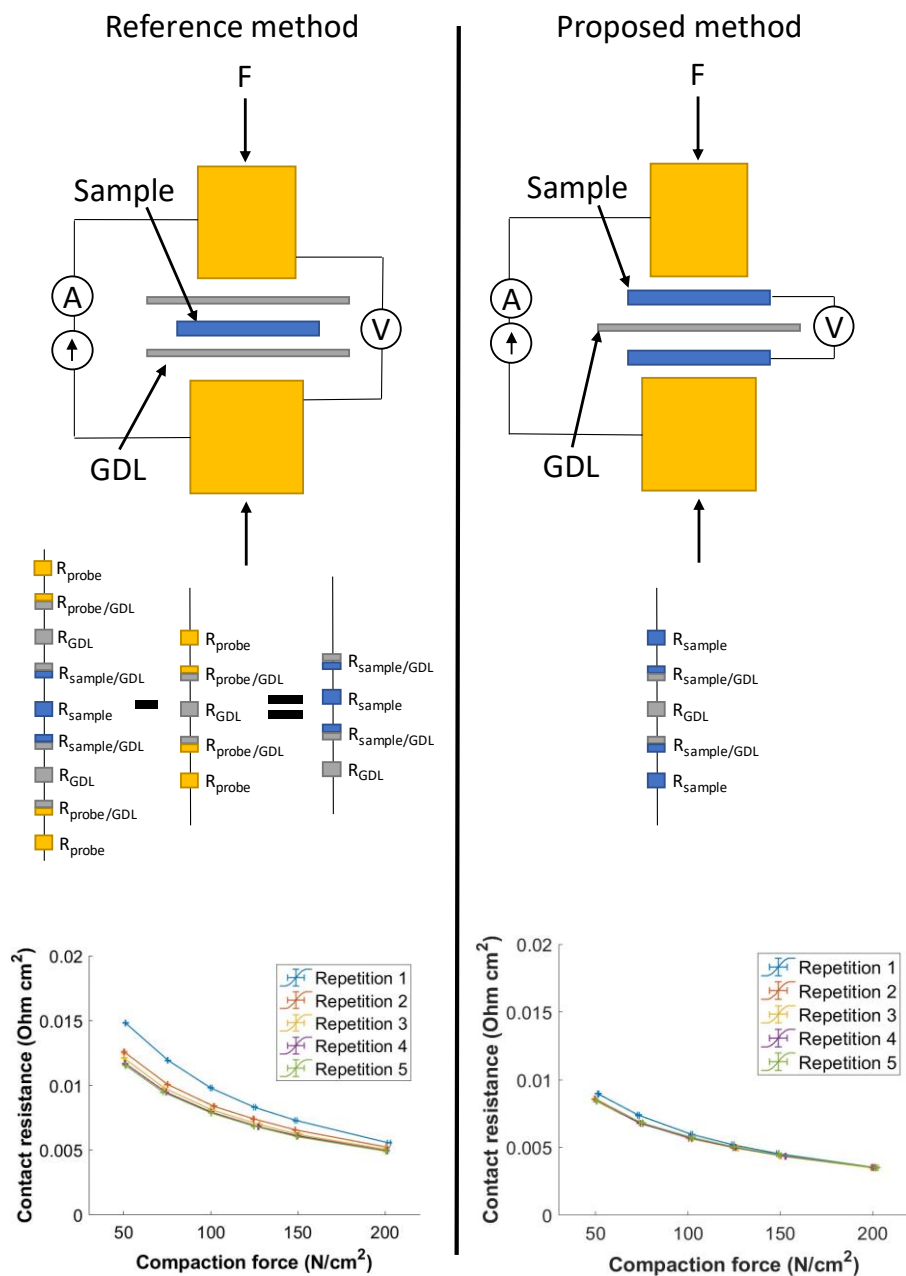


*Figure 27: Schematic illustration and comparative measurements of the reference method and the proposed method.*

#### 4.2.3. *Initial coating comparison*

The ICR measurement of all coated samples towards the GDL can be seen in Figure 28. In these measurements, one GDL is sandwiched between two coated samples. Only the side towards the GDL is coated for the coated stainless steel. It is clear that of all the different coated materials, Au-coated Al has the lowest contact resistance. Al coated with NiP and NiSn and stainless steel with the pure CrFeNi coating follow and are all in the same range. With the addition of Ta to the CrFeNi coating on the stainless steel, the ICR increases, but both 15% Ta and 25% Ta have lower ICR than the stainless-steel substrate, while the pure Ta coating has the highest ICR of all samples.

Interestingly, there is a trend where increasing ICR show increasing measurement uncertainty. For all coatings, three separate sets of samples are tested, and each set contains two coated samples. Hence, the reported curves are an average of six samples. Based on the raw data, it appears that there is a larger likelihood of outliers for the more passive materials. For the pure tantalum coating, one set of samples measures close to the stainless steel, hence the large error bars.

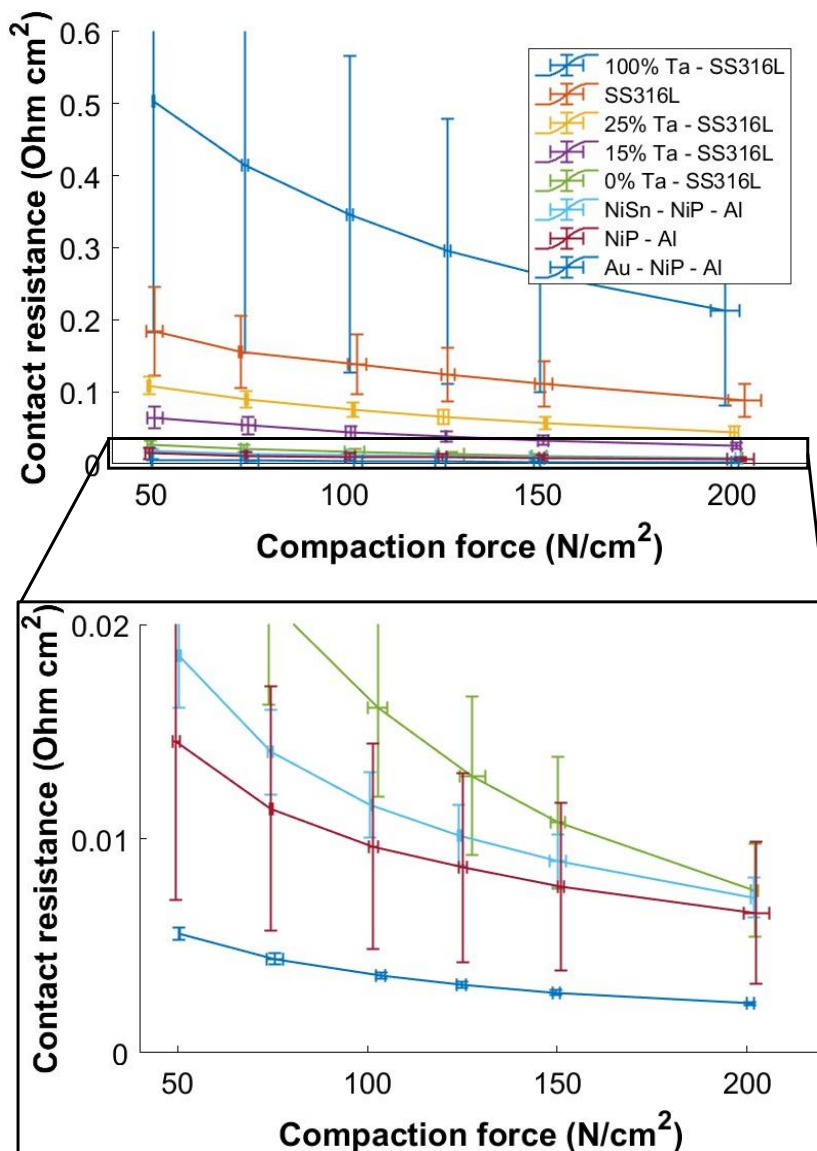


Figure 28: The ICR measurements of all coated samples studied towards the GDL. The coating layers from top to bottom are given, ending with the substrate. For the CrFeNi with added Ta, the wt% of Ta is given.

#### 4.2.4. Ageing CrFeNiTa in H<sub>2</sub>SO<sub>4</sub>

The coatings on stainless steel were stability tested in 0.05 M H<sub>2</sub>SO<sub>4</sub>, first at 0.6 V to simulate the PEMFC conditions and subsequently at 1.5 V vs Ag/AgCl to also assess the suitability of the coatings for PEM water electrolyzers. Both potentials were held for 15 minutes. As is shown in Figure 29a, the pure Ta coating shows an initial peak in current during the hold at 0.6 V, but after 120 seconds, all samples show stable current. When the potential is increased to 1.5 V, the sample with 0% Ta shows a significantly higher current for the first 150 seconds (out of bounds of the graph) before stabilising at around 1 mA/cm<sup>2</sup>, a similar current density to the substrate (Figure 29b). The samples with Ta addition show stable passive behaviour also at 1.5 V.

From the ICR measurements (Figure 29c), it seems that the original oxide layer of the substrate material is dissolved during the hold at 0.6 V, as the ICR is reduced. The ICR of the samples with 0 to 25% Ta increase by 33 to 48%, while the ICR for the pure Ta almost double after the hold at 0.6 V. The ICR of the sample with the 0%Ta coating is similar to the substrate material after the hold at 1.5 V. The SEM and XPS analysis confirm that the high current peak at the beginning of the hold at 1.5 V represents the dissolution of the coating (Figure 29d). Thus, the final ICR measurement is of the substrate also for this sample. The ICR for the samples with 15 and 25% Ta increases significantly after the hold at 1.5 V, and XPS of the surface post-mortem show an enrichment of Ta in the oxide layer.

Overall, the results show that the CrFeNi coating with the addition of Ta can be stabilised in acidic environments more aggressive than what can be found in the PEM cells. The stabilisation is a result of Ta enrichment in the oxide layer. However, the contact resistance of the coated samples is comparable to the substrate after 0.6 V, and increases significantly after being exposed at 1.5 V. Thus, further alloy development or an additional, e.g., carbon-based top coating, is needed to ensure also the low ICR required.

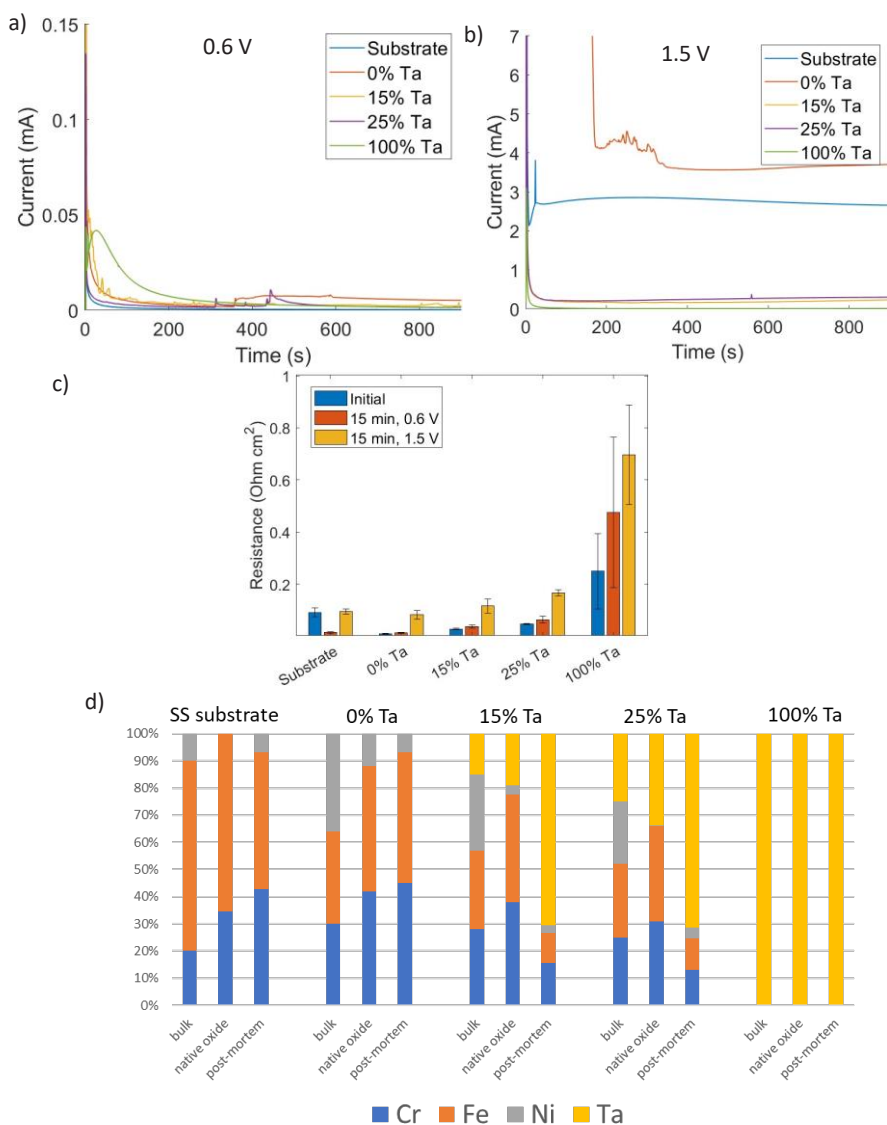


Figure 29: a and b) the potentiostatic hold in 0.05 M  $H_2SO_4$  at 0.6 and 1.5 V, respectively. c) the ICR value at 150 N/cm<sup>2</sup> for all samples initially and after the two potentiostatic holds. d) the composition of the bulk coating, and surface oxide prior to ageing and after both potentiostatic holds, determined by XPS for the oxide and EDS for the bulk.

#### 4.2.5. Ageing NiP and NiSn by environmental durability testing

The current collector plate is, as is shown in Figure 2, at the end of the stack, and connects to the back of the last bipolar plate, as well as to the power terminal through a screw connection. It is assumed that the pH at the current collector plate is neutral. The temperature will, on the other hand, follow the stack. Furthermore, impurities in the air from the environment around the stack may greatly influence the degradation of the power terminal. Environmental durability standards are therefore applied instead of ageing in  $H_2SO_4$  for the Al coated with NiP and NiSn as these materials have been chosen with the current collector as application. Initial measurements of the ICR were performed between two coated samples, both in the test rig and in the prototype screw connection. The sample-sample ICR show the same trend between the coatings as the sample-GDL ICR. The Au coating gives the lowest, followed by NiP, while NiSn has the highest initial ICR (Figure 30).

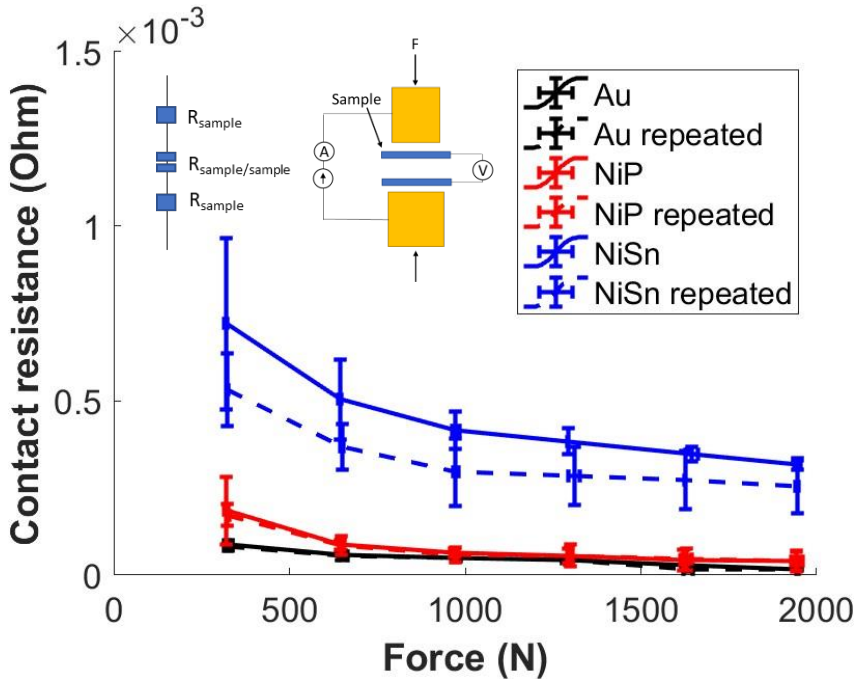
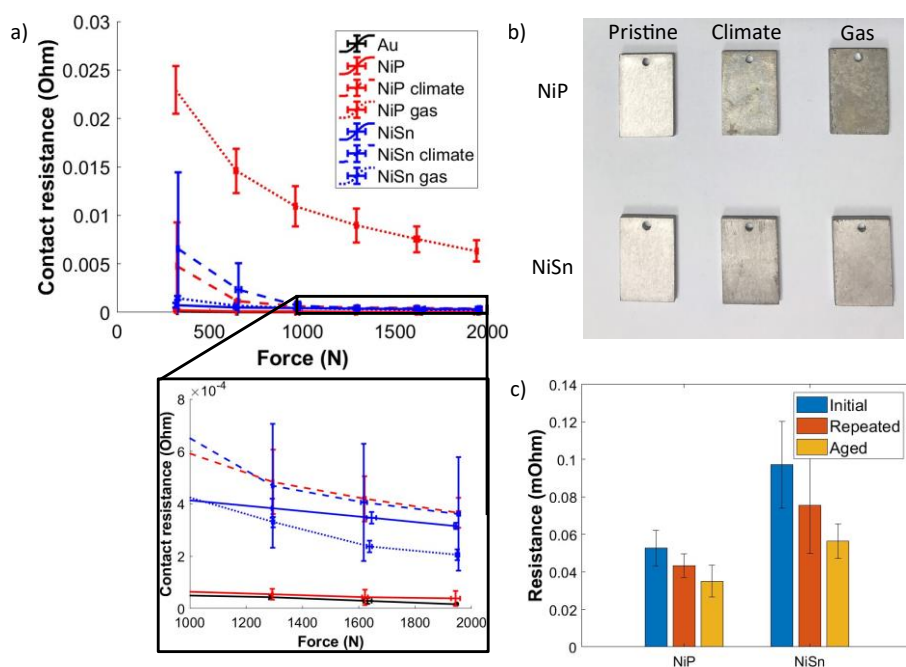


Figure 30: ICR measurements of the pristine samples. The schematic illustration shows the measurement set-up.

To assess the suitability of these coatings for the power connection, two environmental durability tests used for automotive and industrial applications has been applied. The first is climate cycling, according to IEC 60068-2-38. The cycle is adapted to the higher operating temperature of the PEMFC. This test is performed both for the samples and the prototype screw connection. After the climate cycling, the NiSn and NiP have similar ICR; the NiP has an increased ICR while the NiSn is unchanged (Figure 31a). As can be seen in Figure 31b, the surface of the NiP and NiSn samples darkens significantly from pristine to after the climate cycle. Interestingly, the trend is the opposite for the screw connection, where the ICR decreases after climate cycling (Figure 31c). Corrosion products are still be observed on the surface of the coated samples in the screw connection, but thermal expansions during the cycle can cause sufficient pressure to penetrate the oxide layer at the contact points, thus decreasing the ICR.



*Figure 31: The ICR between two coated samples initially and after durability testing in climate cycle and mixed gas exposure.*

The samples furthermore were subjected to mixed gas cycling. Method 4, the most aggressive cycle, has been chosen from the IEC 60068-2-60. A significant increase in ICR is observed for the NiP coating, while the coating with NiSn still appears unchanged. It is evident from Figure 30b that the NiP visually appear darker after exposure to mixed gases, while the NiSn looks similar after the two different environmental durability tests. This shows that the NiSn passive layer is more electrically conductive than the NiP passive layer after environmental durability testing.

#### **4.2.6. *Conclusions on ICR measurements and the effect of passivation on the ICR***

Research question 2 focuses on how to reliably and validly measure the ICR. The results show that the uncertainty due to differences between pieces of the GDL can be reduced by performing several consecutive compressions. By switching the order of the GDLs and samples, a reduced number of consecutive compressions are needed. It furthermore enables ICR measurements of the PVD-coated stainless steel that was only coated on one side of the sample. In contrast to the reference method, the ICR is obtained by a direct measurement instead of calculated from the difference between two measurements. This both simplifies the measurement and reduces uncertainties.

In addition to measuring the samples in their initial state, ageing both in sulfuric acid and according to environmental durability standards was performed. In both cases, the importance of choosing the most similar durability test to the real application is demonstrated as samples showing the lowest increase in ICR after the mildest of the tests failed entirely in the more aggressive test.

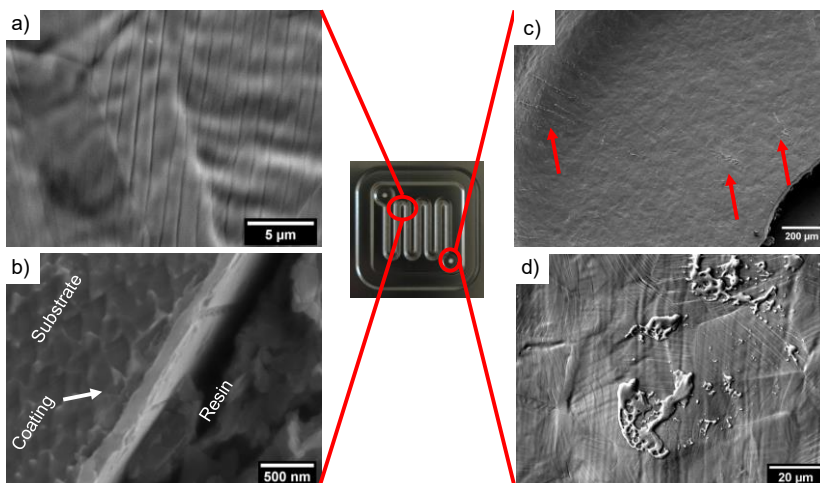
## 4.3. Localised corrosion on bipolar plates

### 4.3.1. *Precoated flow plates*

#### Characterisation

The flow plates with the commercial Sandvik Sanergy LT coating that has been hydroformed are studied in paper 5. SEM analyses performed both on the top and the etched cross-section are shown in Figure 32. EDS results indicate that the coating contains C and Ti. From the top view, parallel lines in the coating with a spacing of 1-2  $\mu\text{m}$  can be seen (Figure 32a). As the coating is thin, the grain structure of the substrate can be seen through the coating. The lines appear to pass grain boundaries without any change in direction on the land area, indicating that these are cracks solely related to the coating. From the cross-section, the bilayer structure of the coating can be seen (Figure 32b), with a total thickness of 100 nm. The cracks primarily penetrate the top layer of the coating, while the bottom layer appears intact or with some necking. At the inlet and outlet (Figure 32d), similar lines can be seen. Here, however, a dependence on the underlying grain structure is seen, and the defects may originate from slip bands in the stainless steel.

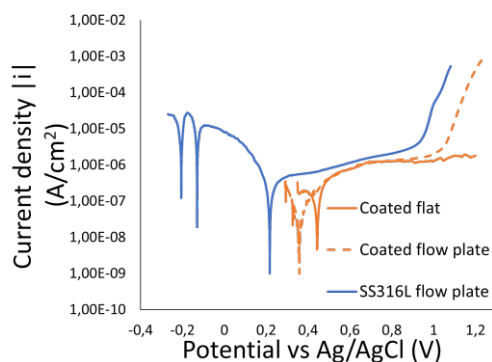
Around the inlet and outlet holes, particles appear on top of the coating (Figure 32 c and d). EDS measurements confirm that these particles have a composition similar to the substrate but with increased oxygen content. Due to the directional distribution of the particles away from the inlet and outlet holes, it is concluded that they originate from laser cutting.



*Figure 32: a) Top view of the land area, b) Cross section of the coating, showing that the top coat layer is cracked while the bottom layer is intact or with only minor cracks, c) and d) the particles on top of the coating close to the laser cut inlet.*

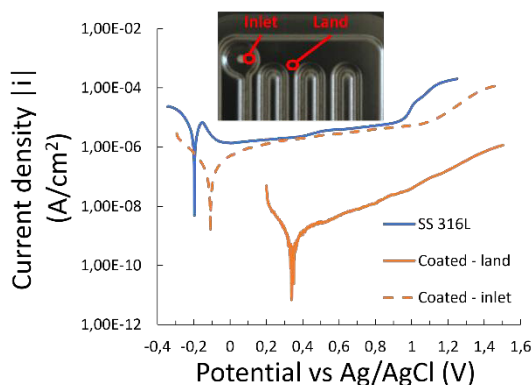
## Electrochemical characterisation

Figure 33 shows the potentiodynamic polarization curves of the coated flow plates, coated flat samples and the uncoated SS316L flow plates. Prior to the polarization curve, the OCP was measured to determine the starting point. The coated plate shows a stable OCP at 0.36 V vs Ag/AgCl, while the stainless-steel plate initially showed an OCP of 0.2 V, but after an hour in the electrolyte, the OCP stabilise at -0.2 V as expected. Still, during the polarization curves, multiple corrosion potentials are observed. The potentiodynamic polarization curves show that the coated flow plate has a higher corrosion potential as compared to bare stainless steel. However, the flat sample shows an even higher corrosion potential, indicating that there are defects in the coated flow plate that causes a mixed potential between the coating and substrate to be measured. Both the coated and bare flow plates show a transpassive behaviour, the bare at 0.9 V and the coated at 1.0 V. The coated flat sample does not show any transpassive behaviour. This again points towards the coated flow plate having exposed substrate, most likely related to the metal droplets at the inlet and outlet and possibly also in the line defects.



*Figure 33: Potentiodynamic polarization curves of the bare and coated flow plate, in addition to the flat coated samples in 0.5 M  $H_2SO_4$ . Measured with a sweep rate of 0.1 mV/s.*

By utilising the electrochemical micro-cell, see Figure 34, it can be seen that the metal oxide particles at the inlet and outlet have similar corrosion potential to stainless steel. In contrast, the land area of the flow plate has a corrosion potential and current density of a protective coating. This confirms that when measuring the whole plate, as is done in Figure 33, a mixed potential between the coating and the droplets at the inlet and outlet is measured.



*Figure 34: The potentiodynamic polarization curves from the electrochemical micro-cell, measured in 0.5 M  $H_2SO_4$  with a sweep rate of 1 mV/s. The placement of the micro-cell can be seen in the inset image.*

## In-situ PEMFC test

Three different load cycles and two different humidity levels were tested to see the effect on the flow plate corrosion. All cells went through multiple shut-downs and start-ups. At each start-up, both sides were purged with nitrogen. No significant difference in PEMFC performance can be seen between the different load cycles (Figure 35). The increased humidity gives better initial performance but quickly results in increased mass transport limitations.

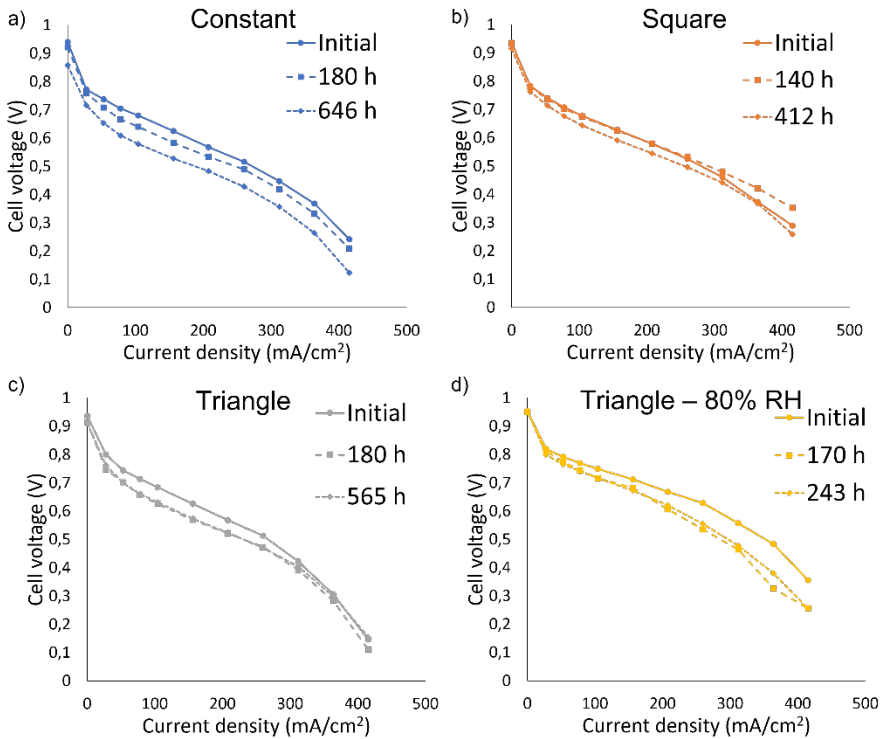


*Figure 35: The PEMFC polarization curves for the cell run with the (a) Constant, (b) Square and (c) Triangle load cycles, and (d) the Triangle load cycle repeated at higher RH. Each potential was held for three minutes, averaging the last minute for the measurement.*

SEM micrographs of the flow plates post-mortem show corrosion attacks on the land areas of the anode plates for all cells. For the cell run at 80% RH, corrosion attacks can also be seen in the flow field. Upon closer inspection, the minor corrosion attacks consist of lines of small circular pits (Figure 36).

The lines appear similar to the lines defects in the coating seen on the land area in Figure 32a. The cracks of the coating run through the centre of the pits, but the rest of the coating appears intact on the surface, with the substrate corroded underneath. This indicates that the corrosion of the substrate is initiated in the cracks. After the initiation of the corrosion, the crack in the coating will limit diffusion to the cavity, and it will continue to grow as a pit. In the more significant corrosion attacks, the pits appear to have grown into each other to form larger trenches and cavities, and the coating is detached due to the lack of a supporting substrate.

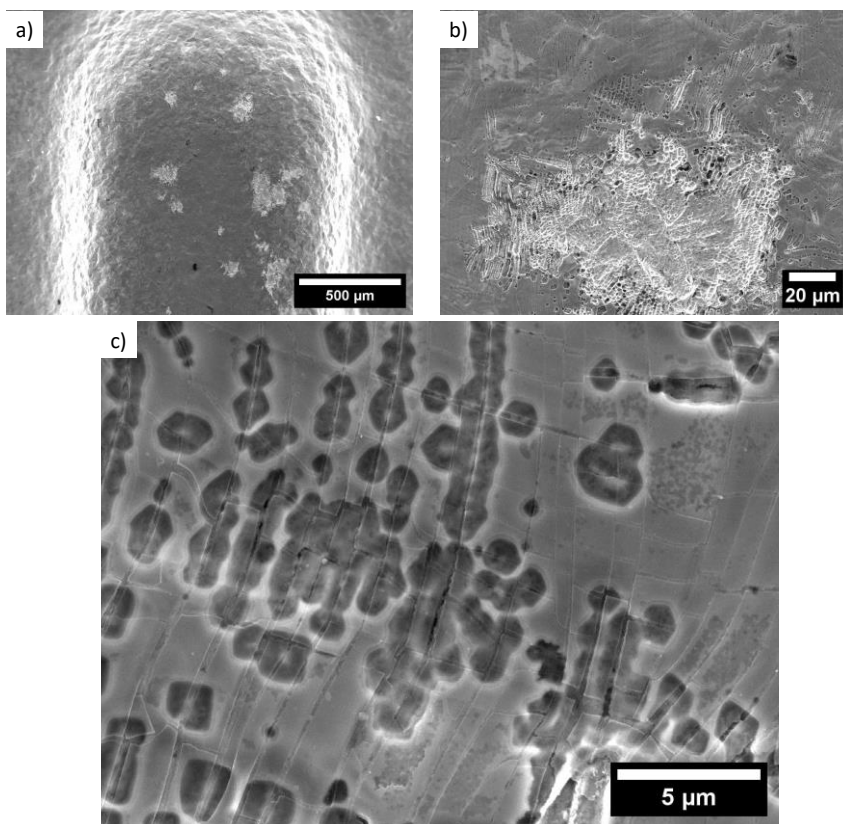


*Figure 36: Overview (a) and close-up micrographs (b and c) of the corrosion attacks on the precoated flow plates on the land area after the constant load cycle.*

The metal droplets at the inlet and outlet that in the electrochemical measurements are pinpointed as a possible source of corrosion do not corrode in the PEMFC. Based on the electrochemical micro-cell results, the potential difference required for galvanic corrosion is present between the droplets and the coating. However, the plates are vertical when mounted in the PEMFC, and it is therefore assumed that there is no water present at the inlet and outlet. As the areas with the droplets do not have contact with the GDL, the same stabilising effect of the pores is not seen, and the droplets are, therefore, not corroded.

### Summarising discussion

From the electrochemical measurements, it is clear that there is a significant difference in corrosion potential between the coating and the substrate. Although the cracks studied by SEM in the cross-section are not penetrating down to the substrate, necking of both coating layers is observed. Thus, cracks penetrating down to the substrate cannot be dismissed when considering the whole plate. The potential of the flow plate in the electrochemical cell indicates a mixed potential between the substrate and the coating. In the PEMFC, where all cells went through start-up and shut-down events, condensation on the flow plate surface is likely. With water on the surface, a crack down to the substrate may cause galvanic corrosion due to the potential difference between the two materials. Since the area of the coating surface is significantly larger than the area at the bottom of the crack, the anodic current density will be equally higher. It appears from the location of the corrosion attacks that the GDL may stabilise water droplets on the surface. It is on the land area, where the flow plate is in contact with the GDL, that the corrosion occurred for the cells run at low relative humidity. After the corrosion is initiated, it continues to grow as a pit. When the relative humidity is increased to 80%, corrosion attacks can be found at the bottom of the flow field as well.

#### 4.3.2. *Laser welded stainless steel*

Welds are required in the bipolar plate active area if the half plates are not coated on both sides. Welds can, however, be a critical point when it comes to localised corrosion due to changes in the microstructure after welding. In the following section, and in paper 6, the corrosion resistance of laser welded stainless steel 304 is studied.

##### Microstructural characterisation

From optical micrographs, it can be seen that the top of the weld forms a wide semicircle, while the bottom has two grooves with a thinner hemisphere in the centre. Furthermore, some particles can be seen on and around the weld at the bottom. The total width of the weld is approximately 150  $\mu\text{m}$ . EBSD of the cross-section shows that the grains go from equiaxed to more columnar grains in the weld (Figure 37), with a line of smaller grains in the centre of the weld. All grains are identified as FCC, so the austenite phase is kept also after the welding process. No compositional change from the bulk material to the weld can be measured by EDS.

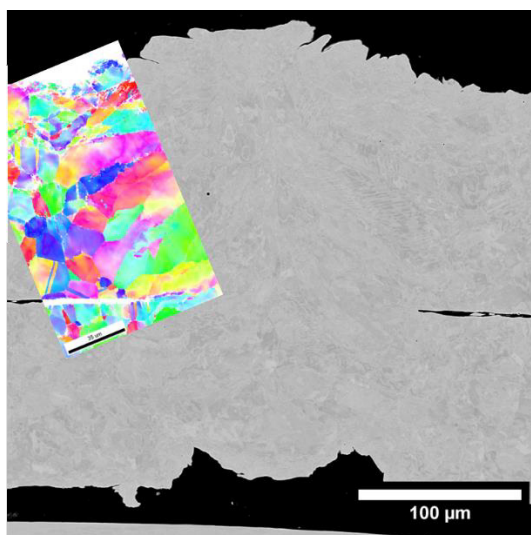


*Figure 37: SEM micrograph of the cross section of the laser weld. The insert is the EBSD scan showing the transition from equiaxed to columnar grains.*

## Potentiodynamic polarization

Potentiodynamic polarization has been performed in the Avesta cell to avoid any crevice corrosion, and the samples were immersed for 24 hours prior to the measurement to ensure that the OCP is stable. The polarization curves of flat stainless steel samples and samples containing the weld have similar OCP (Figure 38), and all show stable passive regions up to 0.8 V vs Ag/AgCl. After 0.8 V, there is a small peak related to the change in the oxidation state of Cr. This peak is larger for the welded samples as compared to the flat. No difference can be seen in the SEM when comparing micrographs from before and after the polarization (Figure 39), indicating that the reaction occurring both in flat and welded samples is related to changes in the passive layer.

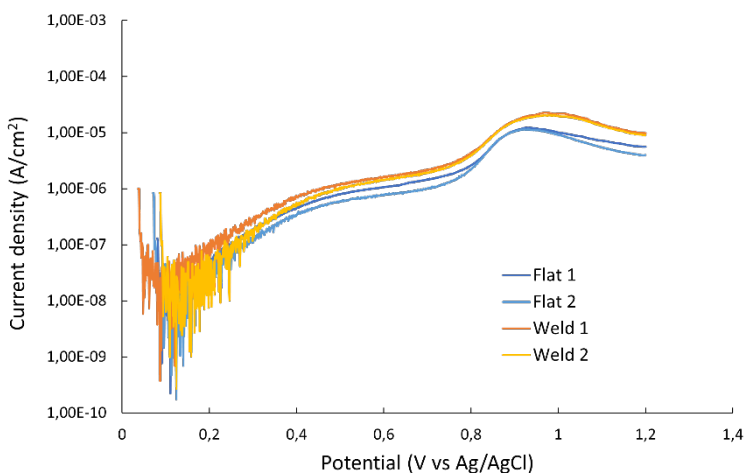


*Figure 38: Potentiodynamic polarization curves of samples both with and without welds. The measurements were performed in an Avesta cell with a sweep rate of 0.1 mV/s, and the electrolyte was 1 mM  $H_2SO_4$  with 2 ppm F.*

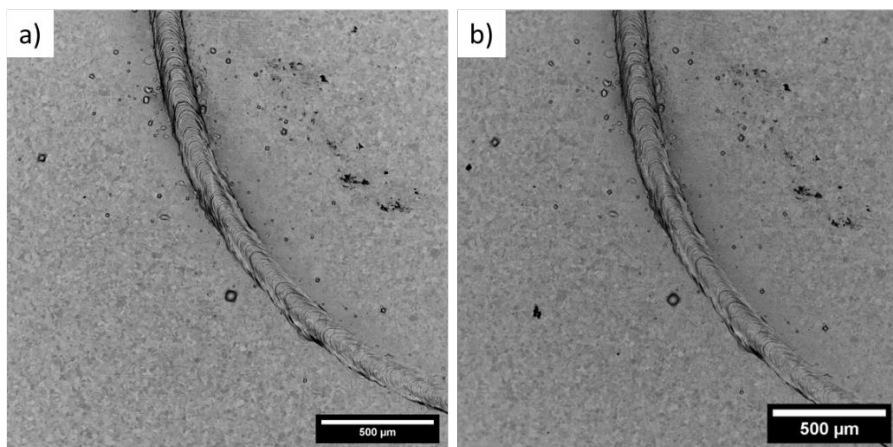


*Figure 39: SEM micrographs of the weld before (a) and after (b) the potentiodynamic polarization.*

### Surface analysis

To understand why no corrosion is observed on the surface after potentiodynamic polarization, and why the current is higher for the sample with the weld, XPS is performed on both pristine and corroded samples. The results show that the weld of the pristine sample has a thicker and more Cr-rich oxide layer as compared to the bulk. After potentiodynamic polarization, the surface of the weld is still more Cr-rich than the bulk, although the difference between the two is smaller. Furthermore, the oxide layer on both the weld and bulk for the corroded sample are thinner than the bulk of the pristine, with the bulk of the corroded sample having the thinnest oxide layer of all studied areas. This does give some explanation as to why no corrosion attacks are seen. The Cr-rich oxide on the weld may, in fact, improve the passivity of the surface. During the potentiodynamic polarization, the thick oxide layer dissolves at the potentials where Cr has a change in oxidation state. Still, both the welded and flat samples showed low current densities even at higher potentials, and no corrosion attacks can be found by SEM. The XPS show that the oxide film is changed so that the oxide film on the weld and bulk are more similar after the corrosion test. All in all, these results do not indicate that exposing a weld in the flow field of a PEMFC will cause corrosion.

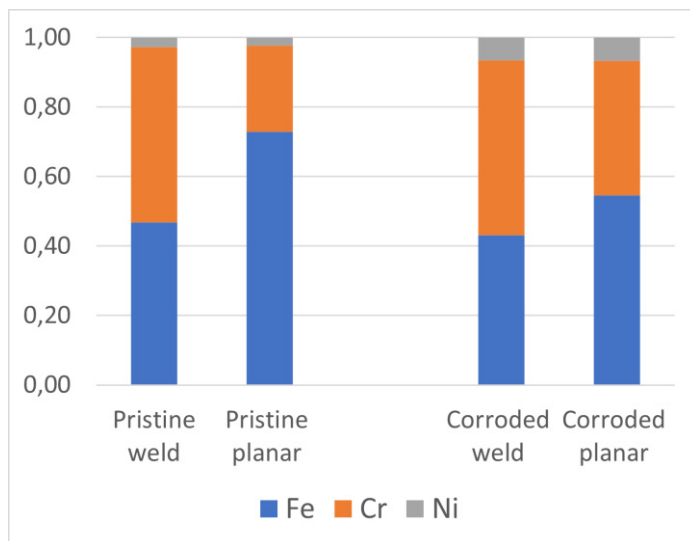


*Figure 40: The surface fraction of Fe, Cr and Ni calculated from the XPS data.*

#### **4.3.3. Conclusions on localised corrosion**

Research question 3 focuses on critical points for localised corrosion on metallic bipolar plates for PEMFCs. In the work performed, three different local defects or critical areas are identified; oxide-containing droplets from laser cutting, cracks in the coating in precoated flow plates, and laser welds.

The oxide-containing droplets corrode when measured in the electrochemical cell and in the electrochemical micro-cell. However, in the PEMFC, the oxide-containing droplets are stable, as there is no water present at the inlet and outlet where these droplets are found. This shows that by correct design, corrosion of these droplets can be avoided.

The cracks in the coating, on the other hand, are not found to be critical in the shorter immersion tests. However, after several hundreds of hours in the PEMFC, corrosion attacks are found on the land areas. The initiation points for the corrosion attacks are identified as the cracks. The rest of the coating remains on top of the corroded substrate until the corroded pit grows so large that the coating has no substrate for support. A mechanism for corrosion

initiation is proposed based on results from both in-situ and ex-situ experiments and analysis after corrosion. In this way, also research question 4 is addressed. This shows that defects in the coating down to the substrate must be avoided and are critical when found on the land. Also here, the solution lies in the correct design to limit the deformation and, by that, avoid defects.

Lastly, laser-welded 304 has been studied. During the welding process, there is a risk of segregation of the alloying elements, and there may be partial oxidation, as was found for the droplets after laser cutting. However, as the laser welding is performed in a protective atmosphere, no difference in composition can be seen, and the oxide layer on the weld is enriched in Cr. The potentiodynamic polarization curves show little difference between samples with and without welds. The laser welds, when performed under a protective atmosphere, do, therefore, not constitute a risk point for localised corrosion in the PEMFC environment.

## 5. Conclusions and future work

A challenge when performing research on complex systems, such as the PEMFC, is to know how to measure correctly, and be sure of what it is that is being measured. In this thesis, focusing on the corrosion of the metallic components in the PEMFC, both the catalyst, bipolar plate, and current collector plate have been studied. In most cases, both ex-situ and in-situ measurements are performed. In several cases, the results from flat samples tested ex-situ differ from the in-situ measurements.

The measurement methodology for the ICR is described only shortly in the literature. Issues such as time dependency and mechanical deformation and relaxation of the GDL can have a great effect on the results from the measurement. Still, the methodology described gives no guidance on how to minimise uncertainties arising from these issues. In paper 3, the mechanical deformation of the GDL and its effect on the ICR are documented. A novel measurement methodology to minimise uncertainties arising from the GDL deformation is suggested. Furthermore, the proposed methodology allows for ICR measurements on samples coated solely on one side and removes the need for subtracting a reference measurement. To conclude, the proposed methodology reduces measurement uncertainty while simplifying the measurement procedure.

The ageing of NiP and NiSn coatings on Al showcases the importance of the correct choice of durability test and the difference between testing flat samples and a prototype. The NiP shows only a slight increase in ICR after the temperature and humidity cycling, and based solely on these results, the additional cost of adding the NiSn may not be needed. However, there is an order of magnitude difference after ageing in a gas mixture, where the NiSn coating is superior. The conclusions from the climate test are, therefore, not valid for the same samples after mixed gas exposure. Furthermore, while there is an increase in ICR for the flat samples after the temperature and humidity cycling, the ICR of the prototype screw connection is reduced. This shows how the corrosion, when isolated, may cause an increase in ICR. Still, when combined with mechanical wear due to the thermal expansion of the components in the screw connection, the trend is the opposite. This shows that

there is a value in making sub-systems in the testing process for new materials for the PEMFC.

For the electrochemical measurements, both different concentrations of  $\text{H}_2\text{SO}_4$  and different potentiostatic holds have been studied. While high potentials have been studied in earlier literature based on measurements over the whole cell, more recent literature points towards the potential being lower on the bipolar plates. The results from paper 4, where one coating shows the lowest increase in ICR after a hold at 0.6 V while the same coating completely dissolves after a hold at 1.5 V, show the importance of not choosing a higher potential than relevant. At the same time, additional in-situ measurements to confirm that the bipolar plate under no circumstance reaches a higher potential are also required to ensure that the test is not too mild.

The electrochemical measurements in papers 5 and 6 are performed at two different concentrations. In both cases, unpolished stainless steel is tested. Even though it is different steel grades, the corrosion potential is expected to be similar. However, the polarization curves look very different between the flow plate in paper 5 and the welded samples in paper 6. When starting to measure the OCP, the potential was relatively high for both samples, around 0.4 V vs Ag/AgCl. However, while the 304 in 1 mM  $\text{H}_2\text{SO}_4$  stabilised at 0.12 V, the OCP for 316L was measured to be -0.2 V in the 0.5 M  $\text{H}_2\text{SO}_4$ , similar to what is measured for polished samples in literature. This shows that the more concentrated solution can break down the passive layer, while measurements in lower concentration measure the passive film. Again, it is important not to choose a more aggressive solution by increasing the concentration and thus lowering the pH, as the electrolyte can destabilise the sample in a way that is not relevant for the PEMFC. At the same time, further studies to ensure that there never is a humid layer on the surface of the PEMFC bipolar plates with lower pH are also needed.

Furthermore, the results have pinpointed some key elements to keep in mind when designing bipolar plates for PEMFCs to avoid corrosion. First of all, defects will form in the coating if it is deformed too much when working with pre-coated materials. Defects penetrating down to the substrate must be avoided. It is, therefore, key to design the flow field to minimise the deformation of the coating, especially on the land areas. Second, around areas

that have been laser cut, particles of the metal that have partially oxidised can be found. These can dissolve upon contact with water inside the PEMFC. It is, therefore, important to optimise the cutting process to minimise the amount of these particles and to design the plates in a way that these particles are outside of the active area of the PEMFC, and at least not on the land area. The latter is the case for the flow plates in the current work, which proved sufficient to avoid corrosion in the PEMFC. Lastly, it is found that the weld in high-quality stainless steel, such as the 316L, is not a source for corrosion in the PEMFC. This opens up the possibility of exposing the bare stainless steel to a much larger degree, although the ICR on the land still needs to be addressed.

As for the catalyst studied in paper 2, the electrodeposition of a ternary alloy is successfully performed. Further optimisation can lead to better control of the alloy composition. The loading of the electrodeposited catalyst is very low, making the measurements in the PEMFC unstable. Literature references have reported higher loading, so here further optimisation is needed for the specific alloy to ensure sufficient loading to get comparable results.

Based on the conclusions from work performed in this thesis, here are some recommendations for future studies:

- Comparative studies of results from ex-situ tests in simulated PEMFC environments with measurements from in-situ PEMFC stacks or short stacks will further confirm the validity of the simulated environments. Most in-situ measurements are performed in single cells, where the flow, current and temperature distributions will differ from the full-scale system.
- Studies comparing ICR measurements with different types of GDLs can further elucidate the impact of GDL on the ICR measurement and on the ICR in the PEMFC.
- Further ICR methodology studies should be performed, comparing results between different measurement setups to validate the proposed methodology further.

- Studies of welded bipolar plates with different types of coatings applied after the welding, both exposing the flow field and with full coverage, can give further input to bipolar plate manufacturing strategies.
- Multicomponent alloys give the possibility of tailoring the properties of the coating, and further studies on alloy development following the principles from paper 4 can result in cost-effective coating for PEMFCs.
- Further studies on how to control the electrodeposition process on the heterogeneous carbon structure of the MPL are needed for more widespread utilisation of electrodeposition as a synthesis method for PEMFC catalysts.

# References

1. Shukla, P. R. *et al.* IPCC, 2022: Summary for Policymakers. In: *Climate Change 2022: Mitigation of Climate Change. Contribution of Working Group III to the Sixth Assessment Report of the Intergovernmental Panel on Climate Change*. (Cambridge University Press, 2022).
2. IEA. *Hydrogen*. <https://www.iea.org/reports/hydrogen> (2022).
3. IEA. *Breakthrough Agenda Report* 2022. <https://www.iea.org/reports/breakthrough-agenda-report-2022> (2022).
4. Cullen, D. A. *et al.* New roads and challenges for fuel cells in heavy-duty transportation. *Nat Energy* **6**, 462–474 (2021).
5. Wang, Y., Chen, K. S., Mishler, J., Cho, S. C. & Adroher, X. C. A review of polymer electrolyte membrane fuel cells: Technology, applications, and needs on fundamental research. *Appl Energy* **88**, 981–1007 (2011).
6. Samsun, R. C., Rex, M., Antoni, L. & Stolten, D. Deployment of Fuel Cell Vehicles and Hydrogen Refueling Station Infrastructure: A Global Overview and Perspectives. *Energies (Basel)* **15**, (2022).
7. Larminie, J., Dicks, A. & McDonald, M. S. *Fuel cell systems explained*. vol. 2 (J. Wiley Chichester, UK, 2003).
8. Yoshida, T. & Kojima, K. Toyota MIRAI fuel cell vehicle and progress toward a future hydrogen society. *Electrochem. Society Interface* **24**, 45–49 (2015).
9. Fernihough, O., Ismail, M. S. & El-kharouf, A. Intermediate Temperature PEFC's with Nafion 211 Membrane Electrolytes: An Experimental and Numerical Study. *Membranes* **12**, 430 (2022).
10. Chandan, A. *et al.* High temperature (HT) polymer electrolyte membrane fuel cells (PEMFC) – A review. *J Power Sources* **231**, 264–278 (2013).
11. Mittal, V. O., Kunz, H. R. & Fenton, J. M. Membrane Degradation Mechanisms in PEMFCs. *J Electrochem Soc* **154**, B652–B656 (2007).
12. Gubler, L., Dockheer, S. M. & Koppenol, W. H. Radical (HO•, H• and HOO•) Formation and Ionomer Degradation in Polymer Electrolyte Fuel Cells. *J Electrochem Soc* **158**, B755–B769 (2011).
13. Gubler, L. & Koppenol, W. H. Kinetic Simulation of the Chemical Stabilization Mechanism in Fuel Cell Membranes Using Cerium and Manganese Redox Couples. *J Electrochem Soc* **159**, B211–B218 (2011).
14. Wong, K. H. & Kjeang, E. Simulation of Performance Tradeoffs in Ceria Supported Polymer Electrolyte Fuel Cells. *J Electrochem Soc* **166**, F128–F136 (2019).
15. Pollet, B. G., Kocha, S. S. & Staffell, I. Current status of automotive fuel cells for sustainable transport. *Curr Opin Electrochem* **16**, 90–95 (2019).
16. Shao, M., Chang, Q., Dodelet, J.-P. & Chenitz, R. Recent Advances in Electrocatalysts for Oxygen Reduction Reaction. *Chem Rev* **116**, 3594–3657 (2016).

17. Omrani, M. *et al.* Platinum group elements study in automobile catalysts and exhaust gas samples. *Environmental Pollution* **257**, 113477 (2020).
18. Chen, D., Kongkanand, A. & Jorne, J. Proton Conduction and Oxygen Diffusion in Ultra-Thin Nafion Films in PEM Fuel Cell: How Thin? *J Electrochem Soc* **166**, F24–F33 (2019).
19. Morgan, J. M. & Datta, R. Understanding the gas diffusion layer in proton exchange membrane fuel cells. I. How its structural characteristics affect diffusion and performance. *J Power Sources* **251**, 269–278 (2014).
20. Okonkwo, P. C. & Otor, C. A review of gas diffusion layer properties and water management in proton exchange membrane fuel cell system. *Int J Energy Res* **45**, 3780–3800 (2021).
21. Mohseninia, A. *et al.* Enhanced Water Management in PEMFCs: Perforated Catalyst Layer and Microporous Layers. *ChemSusChem* **13**, 2931–2934 (2020).
22. Simon, C., Kartouzian, D., Müller, D., Wilhelm, F. & Gasteiger, H. A. Impact of Microporous Layer Pore Properties on Liquid Water Transport in PEM Fuel Cells: Carbon Black Type and Perforation. *J Electrochem Soc* **164**, F1697–F1711 (2017).
23. Mohseninia, A. *et al.* PTFE Content in Catalyst Layers and Microporous Layers: Effect on Performance and Water Distribution in Polymer Electrolyte Membrane Fuel Cells. *J Electrochem Soc* **168**, 034509 (2021).
24. Khedekar, K. *et al.* Effect of Commercial Gas Diffusion Layers on Catalyst Durability of Polymer Electrolyte Fuel Cells in Varied Cathode Gas Environment. *Small* 2201750 (2022).
25. Shaigan, N., Yuan, X.-Z., Girard, F., Fatih, K. & Robertson, M. Standardized testing framework for quality control of fuel cell bipolar plates. *J Power Sources* **482**, 228972 (2021).
26. Asri, N. F., Husaini, T., Sulong, A. B., Majlan, E. H. & Daud, W. R. W. Coating of stainless steel and titanium bipolar plates for anticorrosion in PEMFC: A review. *Int J Hydrogen Energy* **42**, 9135–9148 (2017).
27. Li, X. *et al.* Transient stainless-steel dissolution and its consequences on ex-situ bipolar plate testing procedures. *Int J Hydrogen Energy* **45**, 984–995 (2020).
28. Mele, C. & Bozzini, B. Localised corrosion processes of austenitic stainless steel bipolar plates for polymer electrolyte membrane fuel cells. *J Power Sources* **195**, 3590–3596 (2010).
29. Hinds, G. & Brightman, E. Towards more representative test methods for corrosion resistance of PEMFC metallic bipolar plates. *Int J Hydrogen Energy* **40**, 2785–2791 (2015).
30. Kumagai, M., Myung, S.-T., Ichikawa, T. & Yashiro, H. Applicability of extra low interstitial ferritic stainless steels for bipolar plates of proton exchange membrane fuel cells. *J Power Sources* **195**, 7181–7186 (2010).
31. Kumagai, M., Myung, S.-T., Asaishi, R., Katada, Y. & Yashiro, H. High nitrogen stainless steel as bipolar plates for proton exchange membrane fuel cells. *J Power Sources* **185**, 815–821 (2008).

32. Kumagai, M., Myung, S.-T., Kuwata, S., Asaishi, R. & Yashiro, H. Corrosion behavior of austenitic stainless steels as a function of pH for use as bipolar plates in polymer electrolyte membrane fuel cells. *Electrochim Acta* **53**, 4205–4212 (2008).
33. Hamann, C. H., Hamnett, A. & Vielstich, W. *Electrochemistry*. (Wiley-VCH, 2007).
34. Kahlert, H. Reference electrodes. in *Electroanalytical Methods: Guide to Experiments and Applications* 291–308 (Springer Berlin Heidelberg, 2010).
35. Netwall, C. J., Gould, B. D., Rodgers, J. A., Nasello, N. J. & Swider-Lyons, K. E. Decreasing contact resistance in proton-exchange membrane fuel cells with metal bipolar plates. *J Power Sources* **227**, 137–144 (2013).
36. Nørskov, J. K. *et al.* Origin of the overpotential for oxygen reduction at a fuel-cell cathode. *J. Phys. Chem. B* **108**, 17886 (2004).
37. Rodgers, M. P., Bonville, L. J., Russell Kunz, H., Slattery, D. K. & Fenton, J. M. Fuel Cell Perfluorinated Sulfonic Acid Membrane Degradation Correlating Accelerated Stress Testing and Lifetime. *Chem Rev* **112**, 6075–6103 (2012).
38. Liu, M., Zhao, Z., Duan, X. & Huang, Y. Nanoscale Structure Design for High-Performance Pt-Based ORR Catalysts. *Advanced Materials* **31**, 1802234 (2019).
39. Shao, M., Peles, A. & Shoemaker, K. Electrocatalysis on Platinum Nanoparticles: Particle Size Effect on Oxygen Reduction Reaction Activity. *Nano Lett* **11**, 3714–3719 (2011).
40. Huang, X. *et al.* High-performance transition metal-doped Pt<sub>3</sub>Ni octahedra for oxygen reduction reaction. *Science* **12**, 1230 (2015).
41. Kong, F. *et al.* Active and Stable Pt-Ni Alloy Octahedra Catalyst for Oxygen Reduction via Near-Surface Atomical Engineering. *ACS Catal.* **10**, 4205 (2020).
42. Kühn, S. *et al.* Concave curvature facets benefit oxygen electroreduction catalysis on octahedral shaped PtNi nanocatalysts. *J. Mater. Chem. A* **7**, 1149 (2019).
43. Gong, W. *et al.* Cross-double dumbbell-like Pt-Ni nanostructures with enhanced catalytic performance toward the reactions of oxygen reduction and methanol oxidation. *Appl. Catal. B* **246**, 277 (2019).
44. Shokhen, V., Strandberg, L., Skoglundh, M. & Wickman, B. Impact of Accelerated Stress Tests on the Cathodic Catalytic Layer in a Proton Exchange Membrane (PEM) Fuel Cell Studied by Identical Location Scanning Electron Microscopy. *ACS Appl. Energy Mater* **2022**, 11200–11212 (2022).
45. Meier, J. C. *et al.* Design criteria for stable Pt/C fuel cell catalysts. *Beilstein J Nanotechnol* **5**, 44–67 (2014).
46. He, W. *et al.* Investigation of multiple commercial electrocatalysts and electrocatalyst degradation for fuel cells in real vehicles. *RSC Adv* **12**, 32374 (2022).

47. Jayasayee, K., van Veen, J. A. R., Hensen, E. J. M. & de Bruijn, F. A. Influence of chloride ions on the stability of PtNi alloys for PEMFC cathode. *Electrochim Acta* **56**, 7235–7242 (2011).
48. Li, B. *et al.* High performance octahedral PtNi/C catalysts investigated from rotating disk electrode to membrane electrode assembly. *Nano Res* **12**, 281–287 (2019).
49. Eiler, K., Suriñach, S., Sort, J. & Pellicer, E. Mesoporous Ni-rich Ni-Pt thin films: Electrodeposition, characterization and performance toward hydrogen evolution reaction in acidic media. *Appl. Catal. B* **265**, 118597 (2020).
50. Suh, W.-K., Ganesan, P., Son, B., Kim, H. & Shanmugam, S. Graphene supported Pt-Ni nanoparticles for oxygen reduction reaction in acidic electrolyte. *Int. J. Hydrog. Energy* **41**, 12983 (2016).
51. Tian, X. *et al.* Engineering bunched Pt-Ni alloy nanocages for efficient oxygen reduction in practical fuel cells. *Science* (1979) **366**, 850–856 (2019).
52. Wang, C., Chen, Z. L., Tao, A. W. & Zhang, H. Optimization of Pt-Ni alloy catalysts synthesized by potentiostatic electrodeposition for cathode in PEMFC. *J Electrochem Energy Convers Storage* **13**, 21001 (2016).
53. Wang, J. *et al.* Highly efficient, cell reversal resistant PEMFC based on PtNi/C octahedral and OER composite catalyst. *Int. J. Hydrog. Energy* **45**, 8930 (2020).
54. Ramaswamy, N. *et al.* Mitigation of PtCo/C Cathode Catalyst Degradation via Control of Relative Humidity. *J Electrochem Soc* **168**, 124512 (2021).
55. Jayasayee, K., van Anh T., D., Verhoeven, T., Celebi, S. & de Bruijn, F. A. Oxygen reduction kinetics on electrodeposited PtCo as a model catalyst for proton exchange membrane fuel cell cathodes: Stability as a function of PtCo composition. *J Phys Chem C* **113**, 20371–20380 (2009).
56. O'Brien, T. E. *et al.* Impact of Carbon Support Structure on the Durability of PtCo Electrocatalysts. *J Electrochem Soc* **168**, 054517 (2021).
57. Sneed, B. T., Cullen, D. A., Mukundan, R., Borup, R. L. & More, K. L. PtCo Cathode Catalyst Morphological and Compositional Changes after PEM Fuel Cell Accelerated Stress Testing. *J Electrochem Soc* **165**, F3078–F3084 (2018).
58. Wang, J. *et al.* A neural-network-like catalyst structure for the oxygen reduction reaction: carbon nanotube bridged hollow PtCo alloy nanoparticles in a MOF-like matrix for energy technologies. *J Mater Chem A Mater* **7**, 19786–19792 (2019).
59. Lindahl, N. *et al.* Fuel Cell Measurements with Cathode Catalysts of Sputtered Pt3Y Thin Films. *ChemSusChem* **11**, 1394 (2018).
60. Chu, T. *et al.* Highly active and durable carbon support Pt-rare earth catalyst for proton exchange membrane fuel cell. *Int. J. Hydrog. Energy* **45**, 27291 (2020).
61. Deng, X. *et al.* Scalable preparation of PtPd/carbon nanowires in the form of membrane as highly stable electrocatalysts for oxygen reduction reaction. *Int J Hydrogen Energy* **44**, 2752–2759 (2019).

62. Lim, J.-E. *et al.* Oxygen reduction reaction on electrodeposited PtAu alloy catalysts in the presence of phosphoric acid. *Appl Catal B* **165**, 495–502 (2015).
63. Zhao, Q. *et al.* Synthesis of a high-performance low-platinum PtAg/C alloyed oxygen reduction catalyst through the gradual reduction method. *New J. Chem.* **44**, 3728 (2020).
64. Zhu, J. *et al.* Facet-controlled Pt-Ir nanocrystals with substantially enhanced activity and durability towards oxygen reduction. *Mater. Today* **35**, 69 (2020).
65. Park, H. *et al.* Binder-coated electrodeposited PtNiCu catalysts for the oxygen reduction reaction in high-temperature polymer electrolyte membrane fuel cells. *Appl Surf Sci* **510**, 145444 (2020).
66. Wang, Z., Yao, X., Kang, Y., Xia, D. & Gan, L. Rational Development of Structurally Ordered Platinum Ternary Intermetallic Electrocatalysts for Oxygen Reduction Reaction. *Catalysts* **9**, 569 (2019).
67. Lin, R., Che, L., Shen, D. & Cai, X. High durability of Pt-Ni-Ir/C ternary catalyst of PEMFC by stepwise reduction synthesis. *Electrochim. Acta* **330**, 135251 (2020).
68. Tu, W. *et al.* Tungsten-Doping-Induced Surface Reconstruction of Porous Ternary Pt-Based Alloy Electrocatalyst for Oxygen Reduction. *Adv. Funct. Mater.* **29**, 1807070 (2019).
69. Shen, X. *et al.* Tuning Electronic Structure and Lattice Diffusion Barrier of Ternary Pt-In-Ni for Both Improved Activity and Stability Properties in Oxygen Reduction Electrocatalysis. *ACS Catal.* **9**, 11431 (2019).
70. Li, M., Lei, Y., Sheng, N. & Ohtsuka, T. Preparation of low-platinum-content platinum-nickel, platinum-cobalt binary alloy and platinum-nickel-cobalt ternary alloy catalysts for oxygen reduction reaction in polymer electrolyte fuel cells. *J. Power Sources* **294**, 420–429 (2015).
71. Dionigi, F. *et al.* Controlling Near-Surface Ni Composition in Octahedral PtNi(Mo) Nanoparticles by Mo Doping for a Highly Active Oxygen Reduction Reaction Catalyst. *Nano Lett* **19**, 6876–6885 (2019).
72. Huang, L., Wei, M., Hu, N., Tsiakaras, P. & Shen, P. K. Molybdenum-modified and vertex-reinforced quaternary hexapod nanoskeletons as efficient electrocatalysts for methanol oxidation and oxygen reduction reaction. *Appl. Catal. B* **258**, 117974 (2019).
73. Zhao, M. *et al.* Facile Synthesis of Pt Icosahedral Nanocrystals with Controllable Sizes for the Evaluation of Size-Dependent Activity toward Oxygen Reduction. *ChemCatChem* **11**, 2458 (2019).
74. Lei, W. *et al.* A general strategy for bimetallic Pt-based nano-branched structures as highly active and stable oxygen reduction and methanol oxidation bifunctional catalysts. *Nano Res.* **13**, 638 (2020).
75. Wang, Z. *et al.* Structurally Ordered Low-Pt Intermetallic Electrocatalysts toward Durably High Oxygen Reduction Reaction Activity. *Adv. Funct. Mater.* **29**, 1902987 (2019).
76. Egetenmeyer, A. *et al.* Pulse electrodeposited cathode catalyst layers for PEM fuel cells. *Int J Hydrogen Energy* **42**, 13649–13660 (2017).

77. Egetenmeyer, A. *et al.* Pulse electrodeposition of catalyst nanoparticles for application in PEM fuel cells. *Trans Inst Met Finish* **95**, 9–19 (2017).
78. Huang, C., Bunmi Odetola, C. & Rodgers, M. Nanoparticle seeded pulse electrodeposition for preparing high performance Pt/C electrocatalysts. *Appl Catal A Gen* **499**, 55–65 (2015).
79. Zhang, X., Huang, X., Hu, W. & Huang, Y. A metal-organic framework-derived Fe-N-C electrocatalyst with highly dispersed Fe-N<sub>x</sub> towards oxygen reduction reaction. *Int. J. Hydrog. Energy* **44**, 27379 (2019).
80. Chen, G. *et al.* Zinc-mediated template synthesis of Fe-N-C electrocatalysts with densely accessible Fe-N<sub>x</sub> active sites for efficient oxygen reduction. *Adv. Mater.* **32**, 1907399 (2020).
81. Wang, Y. & Berthon-Fabry, S. One-Pot Synthesis of Fe-N-Containing Carbon Aerogel for Oxygen Reduction Reaction. *Electrocatalysis* **12**, 78 (2021).
82. Reshетенко, T. *et al.* The Effect of Proton Conductivity of Fe-N-C-Based Cathode on PEM Fuel cell Performance. *J. Electrochem. Soc.* **167**, 84501 (2020).
83. Kumar, K. *et al.* On the Influence of Oxygen on the Degradation of Fe-N-C Catalysts. *Angew. Chem. Int. Ed.* **59**, 3235 (2020).
84. Gao, L. *et al.* Hydrogen etching induced hierarchical meso/micro-pore structure with increased active density to boost ORR performance of Fe-N-C catalyst. *J. Energy Chem.* **35**, 17 (2019).
85. Zhang, X. *et al.* Molecular-level design of Fe-N-C catalysts derived from Fe-dual pyridine coordination complexes for highly efficient oxygen reduction. *J. Catal.* **372**, 245 (2019).
86. Wang, R. *et al.* ZIF-derived Co-N-C ORR catalyst with high performance in proton exchange membrane fuel cells. *Prog. Nat. Sci.* **30**, 855 (2020).
87. Cheng, Q. *et al.* Co nanoparticle embedded in atomically-dispersed Co-N-C nanofibers for oxygen reduction with high activity and remarkable durability. *Nano Energy* **52**, 485–493 (2018).
88. Liu, J. *et al.* Metallic cobalt nanoparticles embedded in sulfur and nitrogen co-doped rambutan-like nanocarbons for the oxygen reduction reaction under both acidic and alkaline conditions. *J. Mater. Chem. A*, **7**, 14291 (2019).
89. Hermann, A., Chaudhuri, T. & Spagnol, P. Bipolar plates for PEM fuel cells: A review. *Int J Hydrogen Energy* **30**, 1297–1302 (2005).
90. Porstmann, S., Wannemacher, T. & Drossel, W. G. A comprehensive comparison of state-of-the-art manufacturing methods for fuel cell bipolar plates including anticipated future industry trends. *J Manuf Process* **60**, 366–383 (2020).
91. Pourbaix, M. *Atlas of Electrochemical Equilibria in Aqueous Solutions*. (National Association of Corrosion Engineers, 1974).
92. de Bruijn, F. A., Dam, V. A. T. & Janssen, G. J. M. Review: Durability and degradation issues of PEM fuel cell components. *Fuel Cells* **8**, 3–22 (2008).
93. Manso, A. P. *et al.* Corrosion behavior of tantalum coatings on AISI 316L stainless steel substrate for bipolar plates of PEM fuel cells. *Int J Hydrogen Energy* **45**, 20679–20691 (2020).

94. Puigdomenech, I. HYDRA (Hydrochemical Equilibrium-Constant Database) and MEDUSA (Make Equilibrium Diagrams Using Sophisticated Algorithms) Programs. KTH Royal Institute of Technology, Stockholm (2016).
95. Möller, P. & Nielsen, L. P. *Corrosion - Theory and Practice*. (Möller & Nielsen, 2022).
96. Xi, T. *et al.* Effect of copper addition on mechanical properties, corrosion resistance and antibacterial property of 316L stainless steel. *MaterSci Eng: C* **71**, 1079–1085 (2017).
97. Baba, H., Kodama, T. & Katada, Y. Role of nitrogen on the corrosion behavior of austenitic stainless steels. *Corros Sci* **44**, 2393–2407 (2002).
98. Wang, H., Sweikart, M. A. & Turner, J. A. Stainless steel as bipolar plate material for polymer electrolyte membrane fuel cells. *J Power Sources* **115**, 243–251 (2003).
99. Cho, K. H., Lee, W. G., Lee, S. B. & Jang, H. Corrosion resistance of chromized 316L stainless steel for PEMFC bipolar plates. *J Power Sources* **178**, 671–676 (2008).
100. Yang, Y., Guo, L. & Liu, H. Influence of fluoride ions on corrosion performance of 316L stainless steel as bipolar plate material in simulated PEMFC anode environments. *Int J Hydrogen Energy* **37**, 1875–1883 (2012).
101. Pakmanesh, M. R. & Shamanian, M. Optimization of pulsed laser welding process parameters in order to attain minimum underfill and undercut defects in thin 316L stainless steel foils. *Opt Laser Technol* **99**, 30–38 (2018).
102. Li, D. G., Chen, D. R. & Liang, P. Influences of plastic strain and strain rate on corrosion behavior of 316L stainless steel in simulated cathodic environment of proton exchange membrane fuel cell. *Int J Hydrogen Energy* **46**, 6239–6250 (2021).
103. Lædre, S., Kongstein, O. E., Oedegaard, A., Seland, F. & Karoliussen, H. The effect of pH and halides on the corrosion process of stainless steel bipolar plates for proton exchange membrane fuel cells. *Int J Hydrogen Energy* **37**, 18537–18546 (2012).
104. Feng, K., Wu, G., Li, Z., Cai, X. & Chu, P. K. Corrosion behavior of SS316L in simulated and accelerated PEMFC environments. *Int J Hydrogen Energy* **36**, 13032–13042 (2011).
105. Davies, D. P., Adcock, P. L., Turpin, M. & Rowen, S. J. Stainless steel as a bipolar plate material for solid polymer fuel cells. *J Power Sources* **86**, 237–242 (2000).
106. Davies, D. P., Adcock, P. L., Turpin, M. & Rowen, S. J. Bipolar plate materials for solid polymer fuel cells. *J Appl Electrochem* **30**, 101–105 (2000).
107. Leng, Y., Ming, P., Yang, D. & Zhang, C. Stainless steel bipolar plates for proton exchange membrane fuel cells: Materials, flow channel design and forming processes. *J Power Sources* **451**, 227783 (2020).
108. Oberg, E., Jones, F. D., Horton, H. L. & Ryffel, H. H. *Machinery's Handbook*. (Industrial Press Inc., 2004).

109. Kumar, A., Ricketts, M. & Hirano, S. Ex situ evaluation of nanometer range gold coating on stainless steel substrate for automotive polymer electrolyte membrane fuel cell bipolar plate. *J Power Sources* **195**, 1401–1407 (2010).
110. Gao, P. *et al.* Electrochemical characteristics and interfacial contact resistance of Ni-P/TiN/PTFE coatings on Ti bipolar plates. *J Solid State Electrochem* **22**, 1971–1981 (2018).
111. González-Gutiérrez, A. G., Pech-Canul, M. A., Chan-Rosado, G. & Sebastian, P. J. Studies on the physical and electrochemical properties of Ni-P coating on commercial aluminum as bipolar plate in PEMFC. *Fuel* **235**, 1361–1367 (2019).
112. Sun, Y. P., Wang, Z., Yang, H. J., Lan, A. D. & Qiao, J. W. Effects of the element La on the corrosion properties of CrMnFeNi high entropy alloys. *J Alloys Compd* **842**, 155825 (2020).
113. Yan, W. *et al.* Corrosion-resistant and interfacial conductive AlTiVCrMo high-entropy alloy and (AlTiVCrMo)<sub>Nx</sub> high-entropy ceramics coatings for surface modification of bipolar plates in proton exchange membrane fuel cells. *J Power Sources* **527**, 231217 (2022).
114. Cantor, B., Chang, I. T. H., Knight, P. & Vincent, A. J. B. Microstructural development in equiatomic multicomponent alloys. *Mat Sci Eng: A* **375–377**, 213–218 (2004).
115. Cooper, L. & El-Kharouf, A. Titanium Nitride Polyaniline Bilayer Coating for Metallic Bipolar Plates used in Polymer Electrolyte Fuel Cells. *Fuel Cells* **20**, 453–460 (2020).
116. Deyab, M. A. Corrosion protection of aluminum bipolar plates with polyaniline coating containing carbon nanotubes in acidic medium inside the polymer electrolyte membrane fuel cell. *J Power Sources* **268**, 50–55 (2014).
117. Mawdsley, J. R. *et al.* Composite-coated aluminum bipolar plates for PEM fuel cells. *J Power Sources* **231**, 106–112 (2013).
118. Kita, S., Uchida, H. & Watanabe, M. Metal separators coated with carbon/resin composite layers for PEFCs. *Electrochim Acta* **53**, 2025–2033 (2007).
119. Mine, E. F., Ito, Y., Teranishi, Y., Sato, M. & Shimizu, T. Surface coating and texturing on stainless-steel plates to decrease the contact resistance by using screen printing. *Int J Hydrogen Energy* **42**, 20224–20229 (2017).
120. Yue, R. *et al.* TiN and TiC as stable and promising supports for oxygen reduction reaction: Theoretical and experimental study. *Appl. Surf. Sci.* **495**, 143620 (2019).
121. Li, J. *et al.* Intergranular passivation of the TiC coating for enhancing corrosion resistance and surface conductivity in stainless-steel bipolar plates. *J Mater Sci* **56**, 8689–8703 (2021).
122. Ren, Y. J. & Zeng, C. L. Corrosion protection of 304 stainless steel bipolar plates using TiC films produced by high-energy micro-arc alloying process. *J Power Sources* **171**, 778–782 (2007).
123. Shi, K. *et al.* Corrosion Behavior and Conductivity of TiNb and TiNbN Coated Steel for Metallic Bipolar Plates. *Appl Sci* **9**, 2568 (2019).

124. Yi, P., Zhu, L., Dong, C. & Xiao, K. Corrosion and interfacial contact resistance of 316L stainless steel coated with magnetron sputtered ZrN and TiN in the simulated cathodic environment of a proton-exchange membrane fuel cell. *Surf Coat Technol* **363**, 198–202 (2019).
125. Orsi, A. *et al.* An investigation of the typical corrosion parameters used to test polymer electrolyte fuel cell bipolar plate coatings, with titanium nitride coated stainless steel as a case study. *J Power Sources* **285**, 530–537 (2015).
126. Nygren, K. *et al.* Influence of deposition temperature and amorphous carbon on microstructure and oxidation resistance of magnetron sputtered nanocomposite CrC films. *Appl Surf Sci* **305**, 143–153 (2014).
127. Li, R. *et al.* CrN/Cr-Coated Steel Plates for High-Temperature Polymer Electrolyte Fuel Cells: Performance and Durability. *J Electrochem Soc* **167**, 144507 (2020).
128. Jin, J., Liu, H., Zheng, D. & Zhu, Z. Effects of Mo content on the interfacial contact resistance and corrosion properties of CrN coatings on SS316L as bipolar plates in simulated PEMFCs environment. *Int J Hydrogen Energy* **43**, 10048–10060 (2018).
129. Feng, K. *et al.* C/CrN multilayer coating for polymer electrolyte membrane fuel cell metallic bipolar plates. *J Power Sources* **222**, 351–358 (2013).
130. Li, H. *et al.* Interface-induced degradation of amorphous carbon films/stainless steel bipolar plates in proton exchange membrane fuel cells. *J Power Sources* **469**, 228269 (2020).
131. Zhang, D., Yi, P., Peng, L., Lai, X. & Pu, J. Amorphous carbon films doped with silver and chromium to achieve ultra-low interfacial electrical resistance and long-term durability in the application of proton exchange membrane fuel cells. *Carbon N Y* **145**, 333–344 (2019).
132. Yi, P., Zhang, W., Bi, F., Peng, L. & Lai, X. Microstructure and properties of a-C films deposited under different argon flow rate on stainless steel bipolar plates for proton exchange membrane fuel cells. *J Power Sources* **410–411**, 188–195 (2019).
133. Novalin, T. *et al.* Concepts for preventing metal dissolution from stainless-steel bipolar plates in PEM fuel cells. *Energy Convers Manag* **253**, 115153 (2022).
134. Müller, M.-V. *et al.* Investigation of the effect of carbon post- vs pre-coated metallic bipolar plates for PEMFCs – start-up and shut-down. *Int J Hydrogen Energy* **47**, 8532–8548 (2022).
135. Liang, P. *et al.* Contact resistance prediction of proton exchange membrane fuel cell considering fabrication characteristics of metallic bipolar plates. *Energy Convers Manag* **169**, 334–344 (2018).
136. Kwok, C. T., Fong, S. L., Cheng, F. T. & Man, H. C. Pitting and galvanic corrosion behavior of laser-welded stainless steels. *J Mater Process Technol* **176**, 168–178 (2006).
137. Lai, R., Cai, Y., Wu, Y., Li, F. & Hua, X. Influence of absorbed nitrogen on microstructure and corrosion resistance of 2205 duplex stainless steel joint processed by fiber laser welding. *J Mater Process Technol* **231**, 397–405 (2016).

138. Holm, R. & Holm, E. *Electric Contact Theory and Applications*. (Springer Verlag, 1967).
139. McCay, K. *et al.* Communication-In Situ Monitoring of Interfacial Contact Resistance in PEM Fuel Cells. *J Electrochem Soc* **168**, 064514 (2021).
140. Lædre, S., Kongstein, O. E., Oedegaard, A., Seland, F. & Karoliussen, H. Measuring In Situ Interfacial Contact Resistance in a Proton Exchange Membrane Fuel Cell. *J Electrochem Soc* **166**, F853 (2019).
141. US Department of Energy (DOE). *Fuel Cell Technologies Office Multi-Year Research, Development, and Demonstration Plan, 3.4 Fuel Cells*. <https://www.energy.gov/eere/fuelcells/downloads/fuel-cell-technologies-office-multi-year-research-development-and-22> (2017).
142. Hinds, G. & Brightman, E. In situ mapping of electrode potential in a PEM fuel cell. *Electrochem commun* **17**, 26–29 (2012).
143. Ovarfort, R. New electrochemical cell for pitting corrosion testing. *Corros Sci* **28**, 135–140 (1988).
144. Andreatta, F. & Fedrizzi, L. The use of the electrochemical micro-cell for the investigation of corrosion phenomena. *Electrochim Acta* **203**, 337–349 (2016).
145. International Electrotechnical Commission. *IEC 60068-2-38: Environmental testing, Part 2-38, Tests - Test Z/AD : Composite temperature/humidity cyclic test*. (2021).
146. International Electrotechnical Commission. *IEC 60068-2-60: Environmental testing, Part 2-60, Tests - Test Ke : Flowing mixed gas corrosion test*. (2015).
147. Tsotridis, G., Pilenga, A., De Marco, G. & Malkow, T. *EU harmonised test protocols for PEMFC MEA testing in single cell configuration for automotive applications; JRC Science for Policy report*. (2015).
148. Bednarek, T. & Tsotridis, G. Assessment of the electrochemical characteristics of a Polymer Electrolyte Membrane in a reference single fuel cell testing hardware. *J Power Sources* **473**, 228319 (2020).
149. Bednarek, T. & Tsotridis, G. Comparison of experimental data obtained using the reference and the single-serpentine proton exchange membrane single fuel cell testing hardware. *Data Brief* **31**, 105945 (2020).
150. Petrone, R., Hissel, D., Péra, M. C., Chamagne, D. & Gouriveau, R. Accelerated stress test procedures for PEM fuel cells under actual load constraints: State-of-art and proposals. *Int J Hydrogen Energy* **40**, 12489–12505 (2015).
151. Chen, H. *et al.* A review of durability test protocols of the proton exchange membrane fuel cells for vehicle. *Appl Energy* **224**, 289–299 (2018).
152. Yeetsorn, R. *et al.* Influence of cycle repetition on stack voltage degradation during fuel cell stress tests. *Fuel Cells* **22**, 85–101 (2022).
153. Bisello, A. *et al.* Mitigated Start-Up of PEMFC in Real Automotive Conditions: Local Experimental Investigation and Development of a New Accelerated Stress Test Protocol. *J Electrochem Soc* **168**, 054501 (2021).
154. Oyarce, A. *et al.* Comparing shut-down strategies for proton exchange membrane fuel cells. *J Power Sources* **254**, 232–240 (2014).

155. Ozden, A., Shahgaldi, S., Li, X. & Hamdullahpur, F. Degradations in the surface wettability and gas permeability characteristics of proton exchange membrane fuel cell electrodes under freeze-thaw cycles: Effects of ionomer type. *Int J Hydrogen Energy* (2018)

## Durability Evaluation of PEM Fuel Cell Components

Proton exchange membrane fuel cells (PEMFCs) are used to convert hydrogen and oxygen to electricity, heat, and water. There are no greenhouse gas emissions, given that the hydrogen is produced from renewable sources, such as water electrolysis from wind, hydro or solar energy. PEMFCs can be found on the commercial market today, predominantly in applications such as forklifts, passenger cars and combined heat and power units. The PEMFC is a new technology, and there are hurdles to overcome, mainly with regard to price and durability.

In this work, two PEMFC components are the main focus: the bipolar plate and the catalyst. For the bipolar plate, the effect of defects from fabrication is investigated to further understand the critical factors for corrosion and how to avoid it. Droplets from laser cutting and cracks in the coating due to the forming of pre-coated plates are both identified as possible sources of corrosion. However, by correct design, both can be avoided or made less critical. Laser welding stainless steel 304 is, on the other hand, found not to be a source of corrosion under simulated PEMFC bipolar plate conditions. Furthermore, tailoring the properties of a multicomponent alloy coating by additions of Ta and W is explored to stabilise the coating at higher potentials in the acidic environment of the PEMFC. Ta is found to achieve a protective passive layer at a lower concentration than W. However, it does significantly increase the interfacial contact resistance. One-step synthesis of a ternary alloy by electrodeposition is studied for the catalyst to allow for facile screening of new alloy compositions, both in- and ex-situ. The ternary alloy gives comparable results to the binary alloy even at lower Pt content.

As the PEMFC has entered the commercial market relatively quickly, there is a lack of standardised tests, both on the component and system level. The procedure for testing the interfacial contact resistance of the bipolar plate is studied in detail, and the methodology is further developed to ensure reliable and comparable results.



LIVE MØLMEN is a PhD student at the Department of Electrification and Reliability at RISE Research Institutes of Sweden in Borås, Sweden. She is enrolled in the PhD program at the School of Engineering at Jönköping University. She holds a M.Sc. degree in Materials Technology from the Norwegian University of Science and Technology. Her research interests lie in the field of materials for energy technology, fuel cells and batteries.